Enhanced Crevice Corrosion of Stainless Steel 316 by Degradation of Cr-containing Hollandite Crevice Former

Xiaolei Guo,[1*] Penghui Lei,[2] Chandi Mohanty,[1] Tiankai Yao,[2] Jie Lian,[2] Gerald S. Frankel[1]

[1]*Department of Materials Science and Engineering, Ohio State University, Columbus, OH 43210, USA*

[2]*Department of Mechanical Aerospace and Nuclear Engineering, Rensselaer Polytechnic Institute, Troy, NY 12180*

Corresponding author: Xiaolei Guo, guo.237@osu.edu

Abstract

This study explores the corrosion interactions between stainless steel 316 (SS316), a candidate nuclear waste canister material, and Cr-containing hollandite ($Ba_{1.15}Cr_{2.3}Ti_{5.7}O_{16}$), a model ceramic nuclear waste form. The two materials were corroded in close proximity in 0.6 M NaCl solution at 90 ºC for 28 days. Severe crevice corrosion was observed on the stainless steel surface after the corrosion experiment, which is likely associated with the rapid accumulation of Cr^{3+} cations originating from both SS316 and the Cr-containing hollandite. The enhanced corrosion of SS316 by the corrosion products of hollandite is quantitatively explained using a classical crevice corrosion model.

Keywords:

Crevice corrosion, stainless steel, hollandite, corrosion interaction, nuclear waste form, high level waste

1. Introduction

High level nuclear waste (HLW) is the byproduct of fission reactions occurring inside nuclear reactors. Part of the HLW in the U.S. is the legacy of defense waste produced in the 20th century.[1] Due to the high radioactivity, these wastes must be properly handled and isolated from human activity until the radioactivity decays to a safe level. However, the disposal of defense waste is a challenge because of the form of the waste (liquids and solids currently stored in underground tanks), the extremely complicated waste chemistry, high radioactivity, and the eventual exposure to an aqueous environment during the geological disposition over a timescale of hundreds of thousands of years. The current plan is to convert this waste into solid state borosilicate glass, thereby reducing the chemical/electrochemical activity of the waste and mobility of the radionuclides. The waste-bearing glass is melted and subsequently cast in stainless steel (SS) canisters for the future disposal in an underground repository.[2, 3] Such processing has been underway for over 30 years in the U.S. and will continue for decades. Wastes that cannot be properly handled with glass melters, such as the strongly heat-generating radionuclides ^{137}Cs, and volatile ^{129}I, will be immobilized in metal or ceramic hosts.[4] Regardless of material, the final waste forms must be stable and resistant to aqueous environments for a geological time scale (>10^5 year).

Synroc (from synthetic rock) is a group of ceramic materials that were created to immobilize HLW.[5] Since the launching of this concept in the 1970s, numerous ceramics, including natural and synthesized ones, have been studied as potential nuclear waste forms. Among the rapidly growing number of materials, hollandite ($Ba_x^{2+}Cs_y^{+}M_{2x+y}^{3+}Ti_{8-2x-y}^{4+}O_{16}$) was developed as a promising nuclear waste form to immobilize Cs waste (^{135}Cs and ^{137}Cs) and the corresponding decay product Ba,[6] because the tunnel structure created by the Ti^{4+} octahedra enables the accommodation of mono- or divalent cations. The chemical durability of hollandite with various compositions has been explored by different researchers.[7-14] For example, Angeli et al. systematically studied the aqueous corrosion behavior of $BaCs_{0.28}Al_{1.46}Ti_{5.72}O_{16}$ at 90 ^{o}C as functions of solution pH, sample surface area to volume ratio (S/V), and exposure time.[8] The authors concluded that the dissolution rate of this hollandite is significantly enhanced at low pH (particularly at pH 1) and high S/V. But in general, this material corrodes at a slow rate (several nm per year), which qualifies it as a promising nuclear waste form. In addition to a high chemical durability, a high resistance to gamma and ion radiation was also reported for hollandite by multiple research groups.[9, 11]

Although extensive efforts have been made to evaluate the chemical durability of various individual ceramic waste forms, few studies address the degradation behavior of these materials in a repository environment that includes an actively corroding metallic canister. Existing studies, primarily concerning metals and glass, show that nearfield corrosion interactions are influenced by multiple factors such as the structure and chemistry of the materials, the environment, and the proximity of the materials in contact.[15]

For example, our prior studies revealed that the localized corrosion of stainless steel (SS) can create an aggressive local environment and subsequently accelerate the corrosion of nearby materials, including borosilicate glass,[16, 17] hollandite,[16] and iodine-containing apatite.[18, 19] In a continuation of this series of efforts, this study provides more details about the synergistic corrosion interactions between the grade 316 stainless steel (SS316) and a Cr-containing hollandite ($Ba_{1.15}Cr_{2.3}Ti_{5.7}O_{16}$). Due to the complexity of material corrosion in the actual repository environment, such as radiation[20-25] and the continuously evolving temperature and solution chemistry,[15, 26] it is not possible to address all problems in one study. The focus of this work is the corrosion of the SS exposed with hollandite in a surrogate aqueous environment at a temperature of 90 ^{o}C, simulating the result of the decay heat generated by the encapsulated waste. The degradation of the adjacent hollandite will be thoroughly described in a follow-up article. The overarching goal is to establish comprehensive and quantitative understanding of the corrosion interactions between SS and hollandite.

2. Experimental Method

2.1 Materials

Non-sensitized SS316 sheets (UNS S31600) were purchased from McMaster-Carr. The nominal composition of the SS316 is given in **Table 1**. A SS316 sheet was cut into specimens with a dimension of 2.5 cm × 2.5 cm × 0.3 cm. The specimens were successively abraded from 180 to 1200 grit with SiC papers under water followed by thorough rinsing in ethanol and DI water. The hollandite samples with a composition of $Ba_{1.15}M^{3+}_{2.3}Ti_{5.7}O_{16}$ (M^{3+} = Al^{3+} or Cr^{3+}) were synthesized via spark plasma sintering as reported in our prior study.[16] The as-fabricated hollandite pellets were abraded to 1200 grit. Due to the limited quantity of material, each pellet, originally in a circular shape (diameter ~1.3 cm), was cut into 4 pieces (**Fig. 1a**) for the corrosion experiments. All hollandite specimens were cleaned with ethanol and DI water before usage. NaCl (Fisher Scientific) solution, along with all other solutions used in this study, were prepared with DI water with an electrical resistivity of 18 MΩ·cm. All solutions used in the present study were naturally aerated.

2.2 Corrosion experiment

SS and $Ba_{1.15}Cr_{2.3}Ti_{5.7}O_{16}$ hollandite (hereafter referred to as Cr-Hol) specimens were pre-wetted with 0.6 M NaCl solution and then brought in direct contact with each other. 0.6 M NaCl is a surrogate for seawater and has been commonly used in metal corrosion studies. The chemistry of the actual solution in the repository environment is much more complicated than the 0.6 M NaCl solution, but the ionic strength is generally lower.[27] Nonetheless, the choice of 0.6 M NaCl was based on a large body of literature showing the successful initiation and propagation of crevice corrosion of SS within a reasonable period of time.[28-

32] The assembly was wrapped with PTFE tape to secure the specimens during corrosion exposure. The non-adhesive PTFE tape was loose enough to allow the electrolyte to access the surfaces of both specimens during corrosion. In a separate control experiment, the Cr-Hol was replaced with $Ba_{1.15}Al_{2.3}Ti_{5.7}O_{16}$ hollandite (hereafter referred to as Al-Hol). Each SS-hollandite assembly, wrapped with PTFE tape, was placed in a perfluoroalkoxy alkane (PFA) reactor containing 200 mL of 0.6 M NaCl solution. To avoid the occurrence of crevice corrosion between SS and the PFA reactor, the SS specimen was placed on top of the hollandite for all experimental groups, so the only tight crevice formed was between SS and hollandite. All reactors were placed in a water bath with the temperature controlled at 90.0 ± 0.1°C. After 28 days of corrosion, the samples were removed from the solution, rinsed thoroughly with DI water, and dried for surface characterization.

Due to the irregular shape of the hollandite specimens, which was difficult to avoid because of the limited quantity of materials, it is not possible to exactly know the diffusion length during the crevice corrosion. Therefore, the minimum distance between the geometric center and the crevice boundary was used as the initial value of diffusion length during the modeling. The average crevice gap was governed by the roughness of the hollandite and stainless specimens. For modeling purpose, a gap size of 10 μm measured from a similar assembly using X-ray tomography [33] was used in this study. The actual crevice gap could be much smaller, so 10 μm is a rather conservative choice, possibly leading to underestimation of the concentrations of ions within the crevice. However, the initial selection of the diffusion length and gap size has a minor effect on the modeling result because the diffusion flux is determined by the minimum crevice gap rather than the average crevice gap, and the effective diffusion length is considerably affected by the precipitation of corrosion products in the confined space. Therefore, adjustments were made to these parameters during the modeling. More details are given in Section 4.1. Despite the irregular shape of hollandite specimens and the uncontrolled crevice gap, crevice corrosion successfully initiated and propagated on the surface of SS in two replicated experiments.

Benchmark leaching experiments were also performed to assess the corrosion rate of stand-alone Cr-Hol and Al-Hol specimens in DI water and 0.01 M HCl. The use of DI water allows a conservative estimation of the initial corrosion rate of hollandite specimens without the interference of external ions. DI water is also a standard testing environment that is often used to assess and qualify the chemical durability of a ceramic waste form. On the other hand, leaching data obtained in 0.01 M HCl can help understand the effect of H^+ ions on the accelerated dissolution of hollandite specimens when crevice corrosion occurs. These bulk immersion experiments were conducted in PTFE containers with a S/V of 0.05 cm^{-1}. The temperature was maintained at 90.0 ± 0.1 °C throughout the experiments for up to 4 days. The leachant was replaced

with fresh original solution at preset time intervals. The chemical composition of the leachant was subsequently analyzed with inductively coupled plasma mass spectrometry (ICP-MS).

2.3 Optical microscopy and optical profilometry

The corrosion morphology of corroded specimens (SS and hollandite) was examined with an optical microscope (Olympus PME 3). Three-dimensional (3D) surface topography of the corroded specimens was acquired with an optical profilometry (Bruker Contour GT). Details of surface characterization through optical profilometry can be found in a prior study.[34] A stitching mode was enabled to collect the surface topography information from a large area.

2.4 Scanning electron microscopy/energy dispersive spectroscopy

The morphology and chemical composition of the pristine Cr-Hol and corroded SS were evaluated with a scanning electron microscope (SEM, Thermo Fisher Scientific Apreo FEG) coupled with an EDAX Octane Elect energy dispersive spectroscopy (EDS) system (AMETEK). The data were collected with a working distance of approximately 10 mm, an acceleration voltage of 15.0 kV, and a beam current of 6.4 nA.

2.5 X-Ray photoelectron spectroscopy

After 28 days of corrosion exposure, the SS specimens were subjected to X-Ray photoelectron spectroscopy (XPS, Kratos) analysis, thus shedding light on the compositional change of the outermost surface layer due to corrosion. The probing depth of XPS is approximately 10 nm. Details of experimental parameters are similar to what were used in a prior study.[18] In brief, monochromatic Al-Kα electrons (1486.6 eV, 120 W) were used as the X-ray excitation source. The pass energy was 20 eV, and the emission current was 10 mA. A bias voltage of 140 V was applied. The acquired data were subsequently analyzed with the CasaXPS software. All spectra were calibrated to the C 1s peak centered at 284.8 eV indicative of adventitious carbon.[35]

2.6 Potentiodynamic polarization

Potentiodynamic polarization was performed on the Cr-Hol sample to assess the electrochemical activity. A pristine Cr-Hol specimen was first encapsulated in epoxy with the back side connected to a copper wire to enable electrical connection. The exposed surface was ground to 1200 grit using a series of SiC papers, then cleaned with DI water and ethanol prior to usage. A standard three electrode setup was utilized. The epoxy-encased Cr-Hol specimen had an exposed area of 1.3 cm^2. A piece of platinum mesh (2.5 cm × 2.5 cm) served as the counter electrode and a saturated calomel electrode (SCE) was used as a reference electrode. The Cr-Hol was first immersed in 0.6 M NaCl solution for 2 hours and then potentiodynamically polarized from the open circuit potential to 2.5 V_{SCE} at a scanning rate of 0.167 $mV \cdot s^{-1}$. Potentiodynamic

polarization was also performed on SS316 in 0.6 M NaCl solution at 90 ºC to determine the passive current density, which was fed into the quantitative model described in the discussion section.

3. Results

3.1 Corrosion morphology of corroded SS

After 28 days of corrosion with Cr-Hol, the corroded SS specimens were removed from the 0.6 M NaCl solution. The surface morphology of the SS was first examined with optical microscopy. As shown in **Fig. 1a**, severe localized damage was observed on the surface of the corroded SS. Dark-color corrosion patterns are clearly visible in multiple areas of the surface, indicating selective surface oxidation or precipitation of insoluble corrosion products. Note that similar morphologies were absent on the control SS specimens corroded with Al-Hol, indicating that the corrosion products of Cr-Hol may have accelerated the corrosion of the SS present nearly. These dark-color corrosion products were not only found near the boundary of the contact area between the SS and Cr-Hol, but also in more remote areas that were exposed to the bulk solution. This corrosion morphology may be associated with the transport and deposition of corrosion products resulting from the corrosion interactions between SS and Cr-Hol. The chemical composition of these dark-color corrosion products was analyzed with XPS, which will be presented in a following section. In addition to the dark-color corrosion product accumulated near the boundary of the contact area, a smaller ring was also identified inside the contact area, which is a characteristic morphology of metal crevice corrosion.[36] This ring exhibits a lighter color compared to the nearby crevice boundary. In addition to the characteristic damage near the border of the contact area, large pits and crevice damage with dimensions on the order of hundreds of μm were also identified inside the crevice (**Fig. 1b**). Morphological characterization via SEM shows that most pits observed inside the crevice center are crystallographic, indicating an activation-controlled mechanism (**Fig. 1c**).

An image of the corroded Cr-Hol is also provided in **Fig. 1a**. Selective corrosion attack was observed near the edge of the specimen and the center area. These areas were in direct contact with the locally attacked areas of the SS, indicating the presence of aggressive local environments in these areas. Such aggressive environments are likely a consequence of the corrosion interactions between SS and Cr-Hol. Note that the Cr-Hol specimens have also been systematically characterized and the results will be reported in a follow-up article.

To illuminate the initiation site of crevice corrosion, the SS specimen corroded with Cr-Hol was also subjected to surface topological analysis via optical profilometry. As shown in **Fig. 2,** large and localized damage was identified in several regions inside the crevice. The largest and deepest pit was found near the center of the crevice. This pit has a diameter of ~700 μm and a depth of ~135 μm and was connected to a

large crevice damage located in its west direction (**Figs. 1b** and **2)**. Additionally, some smaller pits were observed near the edge of the crevice. These observations indicate that there were probably more than one initiation sites of localized corrosion. The detail corrosion mechanism will be discussed in a following section.

The boundary of the contact area was further examined with SEM. As shown in **Fig. 3a**, a large amount of corrosion products was found along the border of the contact area. Pits with diameter on the order of tens of μm were identified near the crevice mouth. Pits without (**Fig. 3b**) and with (**Fig. 3c**) a pit cover (a remnant of the passive film) were both identified. A magnified view of the crevice boundary is provided in **Fig. 3d**. In this image, the region to the bottom left was inside the crevice, while the top right was outside the crevice. As shown in **Figs. 3a** and **3d**, numerous cracks, likely formed during sample dehydration in the SEM chamber, exist in the layer of corrosion products built up near the crevice mouth. In certain areas, this thick layer of corrosion products partially detached from the surface, exposing the pristine SS substrate (**Fig. 3d**). An EDS line scan (along the dark blue arrow in **Fig. 3e**) was performed across the border of the crevice, revealing that the corrosion products accumulating along the boundary are enriched in Cr, so are likely Cr oxides or hydroxides. In this area, the concentration of Cr is consistently higher than Fe, except for the cracked regions where the metal substrate was exposed. At the end of the line scan, the concentration of Fe increased to a level similar to that of Cr, suggesting that the Cr-rich precipitation surrounding the crevice boundary originated from the local crevice solution. In an area far away from the crevice that was exposed to the bulk solution during the corrosion test and does not contain dark-colored corrosion products, a large amount of granular corrosion products exists (**Fig. 3f-g**). An EDS map collected from this area suggests that the granular corrosion products are primarily Fe oxides. The Cr, Ni, and Mo signals primarily came from the underlying substrate that was not fully covered by the corrosion products (**Fig. 4**).

In contrast to the SS corroded with Cr-Hol, no visible corrosion attack was found on the SS corroded with Al-Hol (**Fig. 5a**). Instead, several micro particles were found near the boundary of the contact area (**Fig. 5b**). EDS mapping of this area suggests that all these particles contain C and O, while some of them contain Al and Ba (**Fig. 5c**). The latter two elements originated from the corrosion of Al-Hol, indicating the precipitation of metal carbonates during corrosion. The carbonate probably originated from dissolved atmospheric CO_2. Since no localized damage was found for either SS or Al-Hol, the presence of the granular corrosion products on the SS surface indicates the dominance of general corrosion for both materials.

3.2 Surface composition of corroded SS

As shown in **Fig. 1a**, severe localize corrosion was found on the SS surface after 28 days of corrosion with Cr-Hol. To illuminate the underlying corrosion mechanism, the chemical composition of the SS surface was further explored with XPS. Areas inside and outside the crevice as illustrated in **Fig. 6** were subjected

to XPS analysis. Cr 2p, Fe 2p, and Mo 3d spectra were acquired from both areas. The results are also given in **Fig. 6**. For the area inside the crevice, two peaks were identified in the Cr 2p 3/2 region. The deconvoluted peak located at 577.0 eV is likely associated with $Cr(OH)_3$[37] or the partially dehydrated form CrOOH[38] in the passive film while the other peak centered at 578.0 eV may be ascribed to $CrCl_3$.[39] For the area outside the crevice, two peaks were also identified in the Cr 2p 3/2 regime. The dominant peak centered at 577.0 eV is again ascribed to $Cr(OH)_3$[37] or CrOOH.[38] Considering the absence of Fe signal in this area indicating the presence of a thick layer of corrosion product, as will be described in the following paragraph, it is unlikely that $Cr(OH)_3$/CrOOH identified here is part of the passive film. Therefore, this species may result from the precipitation of dissolved Cr^{3+} ions transporting from the crevice area toward the bulk solution due to the increased pH. The other peak with a higher binding energy of 578.8 eV may be associated with CrO_4^{2-}.[40]

For the area inside the crevice, both metallic Fe and Fe_2O_3 species were identified in the Fe 2p 3/2 core level spectrum. In comparison, no Fe signal was detected in the area exposed to the bulk solution during corrosion. This suggests that the SS substrate in the dark-color area was covered by a thick layer of corrosion products that does not contain Fe. Note that this area is not the same as the one examined with EDS mapping (**Fig. 4**), which does not contain the dark-color corrosion products. Combining the observations of SEM and XPS, it is clear that the dark-color corrosion products shown in **Fig. 1a** are primarily Cr oxides and/or hydroxides.

It is worth noting that only the highest oxidation state of Mo (MoO_3) was identified for the area inside the crevice. The two peaks centered at 232.4 and 235.6 eV correspond to the Mo 3d 3/2 and 5/2 core level spectrum, respectively.[41] This is expected because MoO_3 is a stable form of oxide that can withstand the acidic environment[42] created by the metal crevice corrosion. In contrast, the overall oxidation state of Mo was lower in the area exposed to the bulk solution. As shown in **Fig. 6**, Mo existed in four oxidation states in the non-contact area, including metallic Mo (227.6 eV),[43, 44], MoO (228.3 eV),[45] Mo_2O_5 (230.8 eV),[44] and MoO_3 (232.3 eV).[44] The Mo oxides with a lower oxidation state are likely caused by the precipitation of corrosion products in this area. As reported by Lu and Clayton,[46] the transpassive potential of pure Mo metal in 0.1 M HCl is about 115 mV_{SCE}, above which high oxidation states of Mo such as Mo(V) and Mo(VI) can form. Therefore, the identification of MoO_3 in the crevice area suggests that the oxygen reduction reaction occurring on the remote cathode polarized the crevice area to a potential exceeding the transpassive potential of pure Mo. The existence of ohmic potential drop inevitably reduces the potential difference between the external cathode and the anode, but the local potential inside the crevice may still be high enough to cause the transpassive oxidation of Mo under the testing condition. Another possibility is that Mo species were oxidized in the air when the crevice was opened after the corrosion

exposure. However, this interpretation is less likely considering the distinct oxidation states observed inside and outside of the crevice, a phenomenon consistently observed in another experiment.[18]

3.3 Electrochemical reactivity of Cr-Hol

Based on the morphological and compositional characterization of the corroded SS surface, it is apparent that the localized corrosion of SS was enhanced due to the crevice formed with Cr-Hol. The accelerated corrosion of SS could potentially be ascribed to crevice corrosion or galvanic corrosion between the SS and Cr-Hol. Therefore, potentiodynamic polarization curve was collected on the pristine Cr-Hol in 0.6 M NaCl to assess whether it is electrochemically reactive. As shown in **Fig. 7**, Cr-Hol only passes tens of pA over the entire potential region examined, indicating that Cr-Hol is electrochemically inactive. The noise in the polarization curve is probably due to instrumental artifacts that are typically observed at such low currents. Since Cr-Hol is not electrochemically active under the testing condition, the possibility of galvanic corrosion between the SS and Cr-Hol was excluded from further analysis.

It is worth noting that Luca et al. corroded $Cs_{0.8}Ba_{0.4}Ti_8O_{16}$ hollandite in dilute nitric acid solutions at 200 ^{o}C and observed an accelerated corrosion phenomenon, which was attributed to the collapse of the tunnel structure promoted by the oxidation of Ti^{3+}.[7] However, this mechanism probably does not explain the accelerated corrosion observed in our study, again due to the lack of electrochemical activity of the hollandite under the testing conditions. Therefore, oxidation induced structure collapse is also excluded from further analysis.

4. Discussion

4.1 Mechanisms of corrosion interactions between SS and Cr-Hol

As demonstrated in **Section 3.3**, Cr-Hol is not electrochemically active, so the accelerated corrosion observed on the SS surface shown in **Fig. 1** was likely due to crevice corrosion rather than the galvanic corrosion between the SS and Cr-Hol, or the oxidation induced structure collapse. Although SS suffered significant crevice corrosion when immersed with Cr-Hol, similar corrosion morphologies were not identified on the SS corroded with Al-Hol. These different corrosion phenomena suggest that the products leached out from Cr-Hol might have promoted the active dissolution of SS, as evidenced by the large pits formed inside the crevice (**Figs. 1-3**). Considering the similar chemical compositions of Cr-Hol ($Ba_{1.15}Cr_{2.3}Ti_{5.7}O_{16}$) and Al-Hol ($Ba_{1.15}Al_{2.3}Ti_{5.7}O_{16}$), any difference in local environment is likely associated with release of Cr^{3+} from Cr-Hol.[16] Furthermore, Cr^{3+} has a larger hydrolysis constant (pK_H = 4.0) than Al^{3+} (pK_H = 5.0)[47], so hydrolysis of Cr^{3+} cations released into the crevice will result in a more acidic local crevice solution. This qualitative description has been proposed in our prior study.[16] In the following

discussion, the classic model of crevice corrosion by Oldfield and Sutton [48] will be adapted to explain the observed experimental phenomena in a quantitative manner.

Metal cations will accumulate in the confined crevice space from slow passive dissolution due to the transport barrier. The pH decrease associated with hydrolysis of metal cations in the crevice can lead to the breakdown of metal passivity and the subsequent onset of active dissolution.[48] For crevice corrosion involving only a passive metal and an inert crevice former, the incubation time of crevice corrosion strongly depends on the passive current density of the metal.[48] For SS316 used in this study, the metal cations accumulated inside the crevice include Cr^{3+}, Fe^{2+}, Ni^{2+}, and Mo^{3+}. Note that Mo can form various species with different oxidation states. For simplicity, only Mo^{3+} is considered in the calculation. The same approach was used in the Oldfield and Sutton model[48]. The choice of Mo species only slightly affects the simulation result because of its low concentration and hydrolysis constant. All these cations (Cr^{3+}, Fe^{2+}, Ni^{2+}, and Mo^{3+}), once generated, tend to hydrolyze, removing OH^- from the solution to form metal hydroxides and thus reduce the local pH. Because Cr^{3+} has the largest hydrolysis constant among all these cations, the degree of acidification depends largely on the amount of Cr^{3+} generated in the local solution.[48] Therefore, the higher concentration of Cr^{3+} in the crevice may explain the enhanced crevice corrosion damage observed on the SS immersed with Cr-Hol. In the following discussion, all metal cations will be considered so the model may be applicable to a broader range of materials in the future.

Consider a crevice formed between SS and an inert material, SS would be the only source of metal cations. The current density associated with each metal cation, i_{M+}, can be calculated via the following equation assuming congruent metal dissolution [48]:

$$i_{M+} = i_p \frac{\mathrm{f}(x)n}{\sum_{y=1}^{m} \mathrm{f}(y)n} \qquad (1)$$

where i_p is the passive current density, f is the fraction of a specific element in the alloy, and n is the charge associated with a given species. For SS316, **Eq. 1** indicates that the production rates of Cr^{3+}, Fe^{2+}, Ni^{2+}, and Mo^{3+} are $0.26i_p$, $0.61i_p$, $0.11i_p$, and $0.02i_p$, respectively. The i_p value was experimentally obtained from a potentiodynamic polarization curve of SS316 in 0.6 M NaCl solution at 90 °C. As shown in **Fig. 8**, the i_p is on the order of 10 μA·cm^{-2}. Therefore, the production rate of Cr^{3+} (i_{Cr}) was estimated to be ~2.6 μA·cm^{-2}. Using this model, it is possible to assess the local solution chemistry at a given time or the time needed to reach a specific solution condition, such as the critical crevice solution (CCS) for depassivation[48].

However, when a passive metal is corroded with another material that can also release metal cations into the crevice solution, such as Cr-Hol, the total production rate of metal cations (i_{total}) should include an additional term (i_{hol}):

$$i_{total} = i_p + i_{hol} \quad (2)$$

Given the extremely high S/V inside a tight crevice and the difficulty of measuring this rate electrochemically, it is challenging to directly probe this i_{hol} value through experiments. However, an estimated value can be achieved by extrapolation from benchmark experiments and existing data in the literature. The detail methodologies are described below.

To first estimate the production rate of Cr^{3+} from Cr-Hol, benchmark experiments were conducted to leach Cr-Hol specimens without the presence of SS in DI water or 0.01 M bulk HCl solution for 4 days. The cumulative concentrations of Cr^{3+} measured from the DI water and 0.01 HCl solution after 4 days of corrosion were 0.95 mg·m^{-2} and 81.64 mg·m^{-2}, respectively. More details on the leaching study can be found in a previous publication.[49] Although Cr-Hol is not electrochemically active and the release of Cr^{3+} is not an electrochemical process, the cumulative concentration of Cr^{3+} originated from Cr-Hol can be converted to an equivalent current density of cation release (i_{hol}) using the following equation:

$$i_{hol} = \frac{I_{hol}}{A} = \frac{Q}{At} = \frac{nF\Delta m}{MAt} \quad (3)$$

where A is the exposed sample area, Q is charge, t is the corrosion time, n is equivalent charge per mole, F is Faraday's constant, Δm is the cumulative mass change of Cr^{3+} cations, which can be measured by ICP-MS, and M is the molecular weight of Cr. Here we assume linear release of Cr^{3+} from the Cr-Hol over time, which is a reasonable assumption for the initial stage of corrosion. The accuracy of this analysis can be further improved by performing more benchmark experiments in various experimental conditions.

Based on **Eq. 3**, the production rate of Cr^{3+} (i_{hol}) from Cr-Hol corroded in DI water and 0.01 M HCl can therefore be calculated to be 1.5×10^{-9} A·cm^{-2} and 1.3×10^{-7} A·cm^{-2}, respectively. It must be emphasized that the S/V used in the benchmark leaching experiment was 0.05 cm^{-1}, which is several orders of magnitude lower than that of the crevice environment. Considering a crevice with a gap size of 10 μm,[33] the S/V can be estimated to be 2×10^3 cm^{-1}. As has been reported by Angeli et al., the release rate of Cs from hollandite almost linearly depends on the S/V (**Fig. 9**).[8] Assuming the release rate of Cr from Cr-Hol follows a similar linear dependency on S/V, we can estimate the i_{hol} inside the crevice to be on the order of 15 μA·cm^{-2} and 1300 μA·cm^{-2} in DI water and 0.01 M HCl, respectively. We again emphasize that this is a rough estimation, so the result can vary with the actual dissolution mechanism (congruent/noncongruent), dissolution rate in the high S/V condition, actual pH environment at different stages of crevice corrosion, and precipitation of secondary phases. Nonetheless, this rough estimation suggests that Cr-Hol can release a considerable amount of Cr^{3+} into the local crevice, thus reducing the incubation time required to reach the CCS and contributing to the subsequent breakdown of metal passivity and the active dissolution. This hypothesis is further supported with a quantitative model described in the following section.

4.2 Simulating incubation time of crevice corrosion

The crevice corrosion model developed by Oldfield and Sutton [48] was adapted to estimate the effect of Cr-Hol on the incubation time required to reach the CCS concentration. The main assumption is that the pH drop inside the crevice is governed by the precipitation of $Cr(OH)_3$, which removes OH^- from water and decreases the pH. The solution pH was stepped from the initial value of 7 to 0.96. The final pH of 0.96 was selected based on the composition of CCS for SS316 [50] and was calculated via OLI^{TM} software (temperature = 25°C, pressure = 1 atm, MSE (H_3O^+ ion) database). Because the CCS was measured experimentally at 25°C, the same temperature was used during the OLI calculation. The choice of this pH does not affect the following calculations. The step size of pH was 0.01, which is the same value used by Oldfield and Sutton.[48] For each ΔpH of 0.01, the concentrations of H^+ and OH^- in the crevice solution were calculated. To reach a specific pH value, the amount of $Cr(OH)_3$ that needs to precipitate from the solution can be calculated. For example, for the pH to drop from 3 to 2, the amount of $Cr(OH)_3$ that needs to precipitate is (10^{-2} mol·L^{-1} - 10^{-3} mol·L^{-1})/3 = 0.003 mol·L^{-1}. After determining the concentrations of H^+ and $Cr(OH)_3$ at a given pH, the concentration of other Cr containing species were calculated based on the reaction equilibria shown in **Table 2**. Assuming congruent dissolution of SS316, the concentrations of other alloy cations such as Fe^{2+}, Ni^{2+}, and Mo^{3+} at the same pH step were calculated. The initial concentrations of Na^+ and Cl^- were both 0.6 M inside and outside the crevice. Similar to Oldfield and Sutton's work, it was initially assumed that all the currents are carried by migration. Convection was ignored, but the contribution of diffusion was estimated after the initial calculation. All the parameters used in this model are summarized in **Table 3**. The diffusivities of all ions were obtained from the OLI^{TM} software, which is different from Oldfield and Sutton's work, where the diffusivities of alloy cations such as Fe^{2+}, Cr^{3+}, Ni^{2+}, and Mo^{3+}were considered to be the same.

After determining the concentrations of all Cr containing species, the total concentration of Cr, $[Cr]_T$, was calculated. The time needed to drop the pH by a particular step, Δt, is given by the following equation:

$$\Delta t = \frac{\Delta[Cr]_T}{R(Cr)} \qquad (4)$$

where $\Delta[Cr]_T$ is the change of total concentration of Cr for each ΔpH and R(Cr) is the production rate of Cr cations from the SS316 and Cr-Hol. R(Cr) with units of mol·L^{-1}·s^{-1} was calculated from:

$$R(Cr) = \frac{i_{Cr} * 1000}{nFx} \qquad (4)$$

For SS316 corroded with an inert crevice former, i_{Cr} is 0.26 i_p or 2.6 μA·cm^{-2} as described in section 4.1. For SS316 corroded with Cr-Hol, i_{Cr} equals to the sum of the equivalent current density of Cr dissolution from the SS316 and Cr-Hol, which is 2.6 μA·cm^{-2} and 15 μA·cm^{-2}, respectively. For Cr-Hol, the production

rate of Cr^{3+} in DI water was used, because the initial solution pH is assumed to be neutral. Additionally, the crevice gap in **Eq. 4** should also be replaced with an equivalent crevice gap due the fact that Cr^{3+} can be released from both materials forming the crevice. For simplicity, a value of $x/2$ was used in this study.[48] To account for migration, the total charge was calculated during each pH fall. The fraction of charge carried by alloy ions (f_M) such as Fe^{2+}, Cr^{3+}, Ni^{2+}, and Mo^{3+} was determined based on their diffusivities and concentrations at the end of each pH decrement. An adjusted time needed to induce this pH change considering migration, Δt_c, was subsequently obtained by dividing Δt with $1- f_M$. The physical meaning of this correction is that, if 50% of alloy ions migrate out of the crevice during each pH decrement, the total time needed to induce this pH change should be doubled.

When all the calculations were completed, the pH inside the crevice was plotted as a function of cumulative time as shown in **Fig. 10a**. For SS corroded with Cr-Hol, it only takes about 1 h to decrease the crevice pH from 7 to 1 under the testing conditions. On the other hand, the same process takes about 12 h for SS corroded with an inert material, signifying the important role of Cr-Hol in the acceleration of SS crevice corrosion. After the initial calculation, diffusion was taken into account by assuming that the concentration of ions falls linearly from the crevice center to the crevice mouth. Note that Cl^- ions tend to migrate from the bulk solution into the crevice during crevice corrosion, but this process is counterbalanced by the Cl^- ions diffusing from the crevice toward the bulk solution. Similar to Oldfield and Sutton, it was assumed that the Cl^- ions diffused out of the crevice combined with the metal cations, and this neutral combination does not contribute to the total current. It was also considered that the diffusion process is substantially restricted by the confined crevice geometry because the diffusion flux is determined by the minimum crevice gap rather than the average crevice gap. Additionally, the large amount of corrosion products precipitated near the crevice mouth as seen in **Figs. 1-3** also reduce the effective crevice gap and increase the effective diffusion length. After accounting for diffusion, the crevice solution pH was plotted again as a function of time as shown in **Fig. 10b**. Due to the large production rate of Cr^{3+} for the SS/Cr-Hol crevice, the incubation time was not significantly influenced after diffusion was considered. For the crevice formed between SS and an inert material, however, the diffusion of metal cations seems to dilute the crevice solution, thereby preventing the crevice solution pH to drop below about 1.1. The observation that severe crevice corrosion did not occur on SS corroded with Al-Hol suggests that the critical pH needed to break down the passive film is below this value.

4.3 Morphology of crevice corrosion

As shown in **Fig. 2**, several locally damaged areas were observed inside the crevice of the SS, indicating the presence of multiple initiation sites of pitting or crevice corrosion. The presence of multiple isolated pits near the crevice center is consistent with the observations from Oldfield and Sutton[51], particularly at

the initiation stage. The occurrence of localized damage in multiple different locations may be partially associated with the heterogeneous release of Cr^{3+} ions from the Cr-Hol due to the presence of defects and inclusions in the as-prepared Cr-Hol substrate (**Fig. 11**). The heterogenous release of Cr^{3+} may lead to the local enrichment of Cr^{3+} ions in the occluded crevice, thereby triggering the permanent breakdown of the passive film and the subsequent active dissolution of the SS substrate at multiple locations. As suggested by Oldfield and Sutton,[51] isolated pits tend to become interconnected as crevice corrosion evolves from the initiation to the propagation stage, a phenomenon also observed in this study. As shown in **Figs. 1b**, the deepest pit on the right-hand side is connected to the large crevice damage on the left-hand side. The deepest pit identified near the crevice center (**Fig. 2**) was probably stabilized by the pit cover, the remnant of which is visible in **Fig. 1b**.

The depth profiles shown in **Fig. 2** shows that the extent of crevice corrosion increases from the center toward the south and west directions. In a study by Lillard et al., crevice corrosion of alloy 625 was found to initiate in the center and propagate toward the mouth.[52] The authors also reported that the depth of the crevice damage increased from the center to the active front, which is similar to the crevice damage observed in this study. Based on this analysis, it is inferred that the crevice corrosion observed in the current study may also have initiated near the center of the crevice as indicated by the white arrow in **Fig. 2**. As the active front moved toward the crevice mouth in the south and west directions, the depth of the crevice damage increased from several μm to tens of μm. It is worth noting that localized corrosion did not initiate exactly at the center of the crevice, probably due to the irregular shape of the shielded area. The same reason might also partially account for the non-uniform distribution of corrosion products along the border of the crevice. It should also be emphasized that the initiation of the large crevice damage might not have occurred until the build-up of the corrosion products near the crevice boundary. The higher amount of corrosion products accumulated along the east boundaries may lead to a higher ohmic potential drop, therefore crevice corrosion preferentially propagated toward the south and west directions.

Combining these observations, it is possible that pitting corrosion occurred first, most likely near the center of the crevice, leading to the generation of a large amount of soluble corrosion products. The propagation of this large pit was likely facilitated by the presence of a pit cover (**Fig. 1b**), which restricts the mass transport out of the pit. At a specific point, the pit grew to an extent and the pit cover was ruptured. The corrosion products resulted from the large pit subsequently transported from the center toward the crevice mouth and precipitated along the crevice boundaries and several remote areas outside of the crevice (**Fig. 1a**) due to the enhanced pH in these regions. After the build-up of corrosion products along the boundaries, crevice corrosion initiated and preferentially propagated toward the south and west directions due to a lower ohmic potential drop in these directions. In addition to the pitting and crevice corrosion occurred near the

center, smaller pits with diameters on the order of tens of μm were also identified near the crevice mouth (**Figs. 3a-c**), probably also because of the lower ohmic potential drop in this area. In comparison, localized corrosion damage only exists near the mouth of the crevice for SS corroded near I-APT[18] or glass[16, 17]. The mechanism accounting for these different corrosion morphologies will be explained below.

Consider a two-dimensional crevice with a circular shape (**Fig. 12a**). The radius of the shielded area is r_w using the terminology of Lillard et al.[53] From Fick's first law, we obtain the flux that describes the diffusive transport of metal cations out of the crevice:

$$flux = -D\frac{C_{surf}-C_{bulk}}{r_1-r_w} \quad (5)$$

where r_1 is distance from any arbitrary point inside the crevice to the center of the crevice, C_{surf} is the concentration of metal cations on the surface at an arbitrary point inside the crevice, and C_{bulk} is the concentration of metal cations in the bulk solution (outside of crevice). Substituting for:

$$flux = \frac{i_{total}}{nF} \quad (6)$$

Assuming $C_{bulk} = 0$, we obtain:

$$\frac{i_{total}}{nF} = \frac{DC_{surf}}{r_w-r_1} \quad (7)$$

Rearranging **Eq. 7** and considering $r_w - r_1 = r_2$, we know:

$$C_{surf} = \frac{i_{total}r_2}{nDF} \quad (8)$$

As discussed in **Section 4.2**, Cr^{3+} cations that came from the SS and Cr-Hol both contribute to i_{total}, so the incubation time for crevice corrosion can be reduced compared to SS corroded with an inert material, or a material that can release inhibitive species into the crevice solution. For example, glass[16, 17] and I-APT[18] can release silicates and vanadates into the local crevice, respectively, thereby reducing the magnitude of i_p. As a result of this inhibitive effect, the crevice corrosion of SS immersed with glass or I-APT is controlled by the ohmic potential drop.[16] This may explain why localized damage was only identified near the boundary of the crevice on the SS corroded with glass or I-APT.

For SS corroded near Cr-Hol, however, no inhibitive species was released from Cr-Hol during corrosion. Based on **Eq. 8**, it is apparent that C_{surf} is the largest at the center of the crevice during the incubation stage of crevice corrosion. The large effective diffusion length for metal cations to diffuse out of the crevice from the center may lead to faster establishment of the CCS needed for passivity breakdown. This mechanism may explain why pitting corrosion and the subsequent crevice corrosion initiated in the center of the crevice

on SS corroded with Cr-Hol. Although pits were also observed near the crevice mouth, their diameters are much smaller, and their occurrence is more likely controlled by the ohmic potential drop.

Once crevice corrosion initiates, it tends to propagate from the center toward the mouth.[53] During the propagation stage, **Eq. 6** no longer holds because the crevice flux is not equal to the surface current density. Instead, current (I_{total}) should be used rather than the current density (i_{total}):

$$\frac{dm}{dt} = \frac{I_{total}}{nF} \quad (9)$$

In this scenario, consider a crevice geometry with a disc shape (**Fig. 12b**). The crevice gap is defined as δ. As crevice corrosion propagates from the center to the mouth, the corroded area behind the active front tends to repassivate,[33, 52, 53] so the active area of crevice corrosion can be simplified to a toroid shape with an inner and outer diameter of r_1 and r_w, respectively. In this case, the equivalent diffusive current associated with metal cations originating from the SS and Cr-Hol can be described as:[53]

$$I_{total} = nFDS_{crev}C_{surf} \quad (10)$$

where D is the effective diffusion coefficient of metal cations in the crevice environment, C_{surf} is the concentration of metal cations at the surface of the active front, and S_{crev} is a shape factor for the toroid defining the crevice geometry[53]:

$$S_{crev} = \frac{2\pi\delta}{\ln\left(\frac{r_w}{r_1}\right)} \quad (11)$$

Combing **Eq. 10** and **11** gives the following equation:

$$I_{total} = nFDC_{surf}\frac{2\pi\delta}{\ln\left(\frac{r_w}{r_1}\right)} \quad (12)$$

During the propagation of crevice corrosion, C_{surf} should fall in the range of CCS $\leq C_{surf} \leq C_{sat}$, where C_{sat} is the concentration of metal cations at a saturation level. As shown in **Fig. 1**, the large pits observed inside the crevice exhibit a crystallographic morphology, indicating an activation/ohmic controlled mechanism, so C_{surf} cannot exceed C_{sat}. The composition of CCS for SS316 was determined previously to be 2.9 M Fe^{2+}, 0.238 M Ni^{2+}, 0.774 M Cr^{3+}, 0.008 M Cu^{2+}, 0.002 M Co^{2+}, and 0.063 M Mn^{2+}.[50] Therefore, the total concentration of metal cations for the CCS of SS316 is 4.0 M.

Thermodynamic calculations via OLI^{TM} software (temperature = 25°C, pressure = 1 atm, MSE (H_3O^+ ion) database) suggest that the composition of the most concentrated crevice solution, before any salt film can precipitate, consists of 3.02 M Fe^{2+}, 0.48 M Ni^{2+}, and 0.83 M Cr^{3+}. Note that other cations are ignored due to their low concentrations. The total concentration of metal cations in a saturated crevice solution is thus approximately 4.3 M, which is not too different compared to the CCS (~4.0 M). As an approximation, we

assume that I_{total} does not strongly depend on C_{surf} during the crevice propagation (**Eq. 12**). In this case, it may be considered that I_{total} depends monotonically on S_{crev} or r_1 during the propagation stage of crevice corrosion. This may explain why the degree of corrosion increased as the crevice corrosion propagated from the center toward the crevice mouth (**Fig. 2**). It is worth noting that both the CCS and C_{sat} values were determined at 25 °C due to the lack of experimental data available at 90 °C. However, these two values should follow the same trend as the temperature increases, so the overall conclusion should be valid.

4.4 Surface chemistry of SS corroded with Cr-Hol

XPS analysis of the SS sample corroded near Cr-Hol (**Fig. 6**) suggests that the oxidation state of Mo is higher in the area located inside the crevice than the area outside, suggesting the formation of less soluble MoO_3 inside the crevice. The higher oxidation state of Mo observed inside the crevice might be associated with the oxidation of Mo to multiple valent states, but only the least soluble corrosion product remained inside the highly acidic crevice space. The observation of MoO_3 inside the crevice for the current study is consistent with the SS corroded near a PTFE crevice former in a similar environment (0.6 M NaCl solution, 90 °C) for the same period of time.[18] When SS corroded near an iodine containing apatite ($Pb_{9.85}(VO_4)_6I_{1.7}$, hereafter referred to as I-APT), however, the oxidation state of Mo inside the crevice was low, similar to what was found in the area exposed to the bulk solution.[18] The lower oxidation state of Mo is likely due to the inhibition of crevice corrosion. Indeed, the corrosion of I-APT created a Pb- and V-enriched film on the surface of nearby SS, thereby suppressing the corrosion interactions between SS and I-APT. In contrast, a similar protective layer does not exist for the SS corroded near Cr-Hol. Instead, the corrosion products of Cr-Hol accelerated the localized corrosion of SS by facilitating the establishment of an acidic local environment. Therefore, the different oxidation states of Mo observed for SS corroded with Cr-Hol and I-APT suggest that the corrosion interactions between SS and ceramics strongly depends on material composition. This conclusion has direct implications for the design and manufacture of ceramic nuclear waste forms with improved compatibility and chemical durability. In particular, elements that can form cations with a strong tendency to hydrolyze may be harmful for the long-term integrity of a waste package and should be minimized or replaced. In contrast, beneficial elements that can inhibit the corrosion interactions between different nuclear waste materials may be intentionally incorporated to the ceramic matrix to improve the corrosion resistance of the waste package.

5. Conclusions

In this work, the corrosion interactions between SS and Cr-Hol were investigated in 0.6 M NaCl solution at 90 °C for up to 28 days. The corroded samples were characterized with optical microscopy, optical profilometry, SEM, EDS, and XPS. The following conclusions are drawn based on the experimental results:

- Corrosion of SS was enhanced by the degradation of Cr-Hol due to the release of Cr^{3+} cations from both materials.
- Cr^{3+} has a large hydrolysis constant so the accumulation of this species can strongly acidify the local crevice solution.
- Crevice corrosion of SS initiated near the center of the crevice and propagated toward the crevice mouth.
- A quantitative model based on a classical crevice corrosion theory can be used to predict the crevice corrosion between SS and Cr-Hol. This approach could also be extended to a broader range of materials designed for the disposal of high-level nuclear waste.

Data availability

The data that support the findings of this study are available from the corresponding author upon request.

CRediT authorship contribution statement

Xiaolei Guo: Conceptualization, Methodology, Investigation, Writing - original draft, Data curation. **Penghui Lei**: Methodology, Investigation, Data curation. **Tiankai Yao**: Methodology, Investigation, Data curation. **Chandi Mohanty**: Methodology, Investigation, Data curation. **Jie Lian**: Conceptualization, Writing - review & editing, Supervision, Resources. **Gerald S. Frankel**: Writing - review & editing, Supervision, Project administration, Funding acquisition, Resources.

Competing interest statement

The authors declare that they have no known competing interests or personal relationships that could have appeared to influence the work reported in this paper.

Acknowledgement

This work was supported as part of the Center for Performance and Design of Nuclear Waste Forms and Containers, an Energy Frontier Research Center funded by the U.S. Department of Energy, Office of Science, Basic Energy Sciences under Award # DESC0016584. The authors would like to thank Yutichai Mueanngern and Dr. Yehia Khalifa from Ohio State University for their assistance with XPS measurement.

Figure Captions

Figure 1. Corrosion morphologies of the stainless steel 316 and Cr-containing hollandite after 28 days of corrosion in 0.6 M NaCl at 90 ^{o}C. **a**) Illustration of corrosion experimental setup (center) and macrographs of corroded stainless steel 316 (left) and Cr-containing hollandite (right). **b**) Scanning electron microscopy image of large pits observed inside the crevice. **c**) Crystallographic morphology observed on the bottom of one large pit.

Figure 2. Surface topography of the stainless steel 316 after corroding with the Cr-containing hollandite in 0.6 M NaCl at 90 ^{o}C for 28 days. The white arrow indicates the initiation site of the crevice corrosion.

Figure 3. Surface characterization of the stainless steel 316 after corroding with the Cr-containing hollandite in 0.6 M NaCl at 90 ^{o}C for 28 days. Scanning electron microscopy image showing **a**) the boundary of the crevice area, **b**) pits near the crevice mouth without a pit cover, **c**) pits near the crevice mouth with a partially collapsed pit cover, **d-e**) boundary of the crevice area with corrosion products partially detached from the metal substrate. Energy dispersive spectroscopy line scan profiles (dark blue arrow) are overlayed on top of the image. The scale bar for d and e is the same. **f**) an area that was exposed to the bulk solution during corrosion. **g**) an enlarged view of a random area selected from **f**.

Figure 4. Scanning electron microscopy image and energy dispersive spectroscopy maps of the stainless steel 316 after corroding with the Cr-containing hollandite in 0.6 M NaCl at 90 ^{o}C for 28 days. The examined area was located outside the crevice without the presence of dark-color corrosion products. The scale bar of 10 μm applies to all the energy dispersive spectroscopy maps.

Figure 5 Scanning electron microscopy image and energy dispersive spectroscopy maps of the stainless steel 316 after corroding with the Al-containing hollandite in 0.6 M NaCl at 90 ^{o}C for 28 days. Scanning electron microscopy image showing **a**) a large area of corroded stainless steel, **b**) an area near the boundary of the crevice area. **c**) energy dispersive spectroscopy maps of the area shown in **b**. The scale bar of 10 μm applies to all the energy dispersive spectroscopy maps.

Figure 6. Macrograph and X-ray photoelectron spectroscopy spectra for the stainless steel 316 after corroding with the Cr-containing hollandite in 0.6 M NaCl at 90 ^{o}C for 28 days.

Figure 7. Potentiodynamic polarization curve of the pristine Cr-containing hollandite collected in 0.6 M NaCl solution. The exposed area was 1.3 cm^{2}.

Figure 8. Potentiodynamic polarization curve of SS316 in 0.6 M NaCl solution at 90 ^{o}C.

Figure 9. Cs Concentration variations in DI water as a function of the sample surface area to volume ratio after 56 days of corrosion. Data reproduced from Angeli et al.[8] with permission. Copyright Elsevier 2008.

Figure 10. Evolution of crevice solution pH as a function of time predicted by an adapted crevice corrosion model proposed by Oldfield and Sutton[48] by considering **a**) migration only, **b**) migration and diffusion.

Figure 11. Scanning electron microscopy images of pristine Cr-containing hollandite.

Figure 12. Schematic illustration of crevice geometry. **a**) cross-sectional view of a two-dimensional crevice formed between stainless steel (SS) and a Cr-containing hollandite (Cr-Hol) used in this study. **b**) three-dimensional view of a toroid-shape crevice formed between SS and Cr-Hol. r_w is the diameter of the circular crevice area. r_1 is the distance between any given point and the center of the crevice. r_2 is the distance between any given point and closest edge of the crevice. δ is the size of the crevice gap. I is the current associated with the diffusive transport of metal cations out of the crevice.

Table 1 Nominal composition of SS316.

	C	Mn	P	S	Si	Cr	Ni	Mo	N	Fe
wt.%	<0.08	<2.00	<0.045	<0.030	<0.75	16.00 - 18.00	10.00 - 14.00	2.00 - 3.00	<0.10	Balance

Table 2 Hydrolysis equilibria of major cations considered in this study. All at 90 °C and determined by OLI software.

$Cr^{3+} + H_2O \rightleftharpoons Cr(OH)^{2+} + H^+$	$K_1 = 1.46 \times 10^{-4}$
$Cr(OH)^{2+} + H_2O \rightleftharpoons Cr(OH)_2^{+} + H^+$	$K_2 = 2.48 \times 10^{-9}$
$Cr(OH)_3\ (s) \rightleftharpoons Cr^{3+} + 3OH^-$	$K_3 = 1.06 \times 10^{-38}$

Table 3 Parameters used in crevice corrosion modeling.

Notation	Parameter	Quantity	Unit	Source
x	Crevice gap	10×10^{-4}	cm	
T	Temperature	90	°C	
c_{O2}	Initial concentration of O_2 in solution	5.09×10^{-5}	$mol \cdot L^{-1}$	Ref [54]
i_p	Passive current density	10×10^{-6}	$\mu A \cdot cm^{-2}$	Experiment
ΔpH	Step of pH changes	0.01	A.U.	
D_{O2}	Diffusivity of oxygen in water at 90 °C	2.20×10^{-5}	$cm^2 \cdot s^{-1}$	Ref [55]
D_{Cr}	Diffusivity of Cr^{3+} ions in water at 90 °C	1.98×10^{-5}	$cm^2 \cdot s^{-1}$	OLI software
D_{Fe}	Diffusivity of Fe^{2+} ions in water at 90 °C	2.33×10^{-5}	$cm^2 \cdot s^{-1}$	OLI software
D_{Ni}	Diffusivity of Ni^{2+} ions in water at 90 °C	2.30×10^{-5}	$cm^2 \cdot s^{-1}$	OLI software
D_{Mo}	Diffusivity of Mo^{3+} ions in water at 90 °C	1.75×10^{-5}	$cm^2 \cdot s^{-1}$	OLI software
D_{Na}	Diffusivity of Na^+ ions in water at 90 °C	4.08×10^{-5}	$cm^2 \cdot s^{-1}$	OLI software
D_{Cl}	Diffusivity of Cl^- ions in water at 90 °C	5.65×10^{-5}	$cm^2 \cdot s^{-1}$	OLI software
n	Equivalents number per mol for oxygen reduction	4	A.U.	
F	Faraday constant	96485	$s \cdot A \cdot mol^{-1}$	

References

[1] S. Gin, A. Abdelouas, L.J. Criscenti, W.L. Ebert, K. Ferrand, T. Geisler, M.T. Harrison, Y. Inagaki, S. Mitsui, K.T. Mueller, J. Marra, C.G. Pantano, E.M. Pierce, J.V. Ryan, J.M. Schofield, C.I. Steefel, J. Vienn, An International Initiative on Long-term Behavior of High-level Nuclear Waste Glass, Mater. Today, 16 (2013) 243-248.

[2] M.I. Ojovan, W.E. Lee, S.N. Kalmykov, An introduction to nuclear waste immobilisation, Elsevier2019.

[3] G.S. Frankel, J.D. Vienna, J. Lian, X. Guo, S. Gin, S.H. Kim, J. Du, J.V. Ryan, J. Wang, W. Windl, Recent Advances in Corrosion Science Applicable To Disposal of High-Level Nuclear Waste, Chemical Reviews, 121 (2021) 12327.

[4] G.S. Frankel, J.D. Vienna, J. Lian, J.R. Scully, S. Gin, J.V. Ryan, J. Wang, S. Kim, W. Windl, J. Du, A Comparative Review of the Aqueous Corrosion of Glasses, Crystalline Ceramics, and Metals, npj Mater. Degrad., 2 (2018) 15.

[5] A. Ringwood, S. Kesson, N. Ware, W. Hibberson, A. Major, Immobilisation of high level nuclear reactor wastes in SYNROC, Nature, 278 (1979) 219-223.

[6] W. Lutze, R.C. Ewing, Radioactive waste forms for the future, New York, 1988.

[7] V. Luca, D. Cassidy, E. Drabarek, K. Murray, B. Moubaraki, Cesium Extraction from $Cs_{0.8}Ba_{0.4}Ti_8O_{16}$ Hollandite Nuclear Waste Form Ceramics in Nitric Acid Solutions, J. Mater. Res., 20 (2005) 1436-1446.

[8] F. Angeli, P. McGlinn, P. Frugier, Chemical Durability of Hollandite Ceramic for Conditioning Cesium, J. Nucl. Mater., 380 (2008) 59-69.

[9] T. Suzuki-Muresan, J. Vandenborre, A. Abdelouas, B. Grambow, S. Utsunomiya, Studies of (Cs, Ba)-Hollandite Dissolution Under Gamma Irradiation at 95 C and at pH 2.5, 4.4 and 8.6, J. Nucl. Mater., 419 (2011) 281-290.

[10] M. Carter, E. Vance, D. Mitchell, J. Hanna, Z. Zhang, E. Loi, Fabrication, characterization, and leach testing of hollandite,(Ba, Cs)(Al, Ti) 2Ti6O16, Journal of Materials Research, 17 (2002) 2578-2589.

[11] A. Abdelouas, S. Utsunomiya, T. Suzuki, B. Grambow, T. Advocat, F. Bart, R.C. Ewing, Effects of ionizing radiation on the hollandite structure-type: Ba0. 85Cs0. 26Al1. 35Fe0. 77Ti5. 90O16, American Mineralogist, 93 (2008) 241-247.

[12] J. Amoroso, J. Marra, S.D. Conradson, M. Tang, K. Brinkman, Melt processed single phase hollandite waste forms for nuclear waste immobilization: Ba1. 0Cs0. 3A2. 3Ti5. 7O16; A= Cr, Fe, Al, Journal of alloys and compounds, 584 (2014) 590-599.

[13] Y. Xu, Y. Wen, R. Grote, J. Amoroso, L. Shuller Nickles, K.S. Brinkman, A-site compositional effects in Ga-doped hollandite materials of the form BaxCsyGa2x+ yTi8− 2x− yO16: implications for Cs immobilization in crystalline ceramic waste forms, Scientific reports, 6 (2016) 1-8.

[14] G.R. Lumpkin, K.L. Smith, M.G. Blackford, Electron microscope study of Synroc before and after exposure to aqueous solutions, Journal of Materials Research, 6 (1991) 2218-2233.

[15] X. Guo, S. Gin, G.S. Frankel, Review of Corrosion Interactions Between Different Materials Relevant to Disposal of High-level Nuclear Waste, npj Mater. Degrad., 4 (2020) 34.

[16] X. Guo, S. Gin, P. Lei, T. Yao, H. Liu, D.K. Schreiber, D. Ngo, G. Viswanathan, T. Li, S.H. Kim, Self-accelerated corrosion of nuclear waste forms at material interfaces, Nature Materials, 19 (2020) 310-316.

[17] X. Guo, S. Gin, H. Liu, D. Ngo, G. Viswanathan, J. Luo, S. Kim, C. Mohanty, J.D. Vienna, J.V. Ryan, G.S. Frankel, Near-Field Corrosion Interactions between Glass and Corrosion Resistant Alloys, npj Mater. Degrad., 4 (2020) 8.

[18] X. Guo, Y. Wang, T. Yao, C. Mohanty, J. Lian, G.S. Frankel, Corrosion Interactions Between Stainless Steel and Lead Vanado-iodoapatite Nuclear Waste Form Part I, npj Mater. Degrad., 4 (2020) 13.

[19] T. Yao, X. Guo, P. Lei, Y. Wang, G.S. Frankel, J. Lian, Corrosion Interactions between Stainless Steel and Lead Vanado-Iodoapatite Nuclear Waste Form Part II, npj Mater. Degrad., 4 (2020) 15.

[20] W. Burns, W. Marsh, W. Walters, The λ irradiation-enhanced corrosion of stainless and mild steels by water in the presence of air, argon and hydrogen, Radiation Physics and Chemistry (1977), 21 (1983) 259-279.
[21] G. Marsh, K. Taylor, G. Bryan, S. Worthington, The influence of radiation on the corrosion of stainless steel, Corrosion science, 26 (1986) 971-982.
[22] R.S. Glass, G.E. Overturf, R.A. Van Konynenburg, R.D. McCright, Gamma radiation effects on corrosion—I. Electrochemical mechanisms for the aqueous corrosion processes of austenitic stainless steels relevant to nuclear waste disposal in tuff, Corrosion Science, 26 (1986) 577-590.
[23] S. Worthington, G. Marsh, K. Taylor, The influence of radiation on crevice corrosion, Improvements in Materials Reliability in the Back End of the Nuclear Fuel Cycle: Proceedings of an IAEA Technical Committee Meeting, 1993, pp. 55-64.
[24] D.W. Shoesmith, F. King, The effects of gamma radiation on the corrosion of candidate materials for the fabrication of nuclear waste packages, Atomic Energy of Canada Limited, 1999.
[25] X. Guo, S. Gin, P. Lei, T. Yao, H. Liu, D.K. Schreiber, D. Ngo, G. Viswanathan, T. Li, S.H. Kim, Reply to: How much does corrosion of nuclear waste matrices matter, Nature Materials, 19 (2020) 962-963.
[26] J.H. Payer, S.A. Carroll, G.E. Gdowski, R.B. Rebak, A Framework for the Analysis of Localized Corrosion at the Proposed Yucca Mountain Repository, Yucca Mountain Project, Las Vegas, NV (United States), 2006.
[27] I.C. Yang, G.W. Rattray, P. Yu, Interpretation of chemical and isotopic data from boreholes in the unsaturated zone at Yucca Mountain, Nevada, US Department of the Interior, US Geological Survey1996.
[28] Z. Szklarska-Smialowska, J. Mankowski, Crevice corrosion of stainless steels in sodium chloride solution, Corrosion Science, 18 (1978) 953-960.
[29] J. Dawson, M. Ferreira, Crevice corrosion on 316 stainless steel in 3% sodium chloride solution, Corrosion science, 26 (1986) 1027-1040.
[30] S. Okayama, Y. Uesugi, S. Tsujikawa, The Effect of Alloying Elements on the Repassivation Potentials for Crevice Corrosion of Stainless Steels in 3% NaCl Solution, Corrosion Engineering, 36 (1987) 157-167.
[31] T. Shinohara, S. Tsujikawa, N. Masuko, In-situ Measurement for Crevice Corrosion of High Purity 18Cr-14Ni Steel under Optical Glass in 3% NaCl Solution, CORROSION ENGINEERING, 39 (1990) 238-246.
[32] Q. Hu, G. Zhang, Y. Qiu, X. Guo, The crevice corrosion behaviour of stainless steel in sodium chloride solution, Corrosion science, 53 (2011) 4065-4072.
[33] R.S. Lillard, D.M. Miller, C.B. Clemons, K.L. Kreider, G.W. Young, Quantifying Alloy 625 Crevice Corrosion using an Image Differencing Technique: Part II. A Diffusive Transport Model of Crevice Cation Concentration using Surface Current Density, J. Electrochem. Soc., 167 (2020) 141503.
[34] C. Li, X. Guo, G.S. Frankel, Corrosion inhibition of AA2024-T3 by smart polyelectrolyte coacervates responsive to both acidic and alkaline environments, Progress in Organic Coatings, 146 (2020) 105719.
[35] X. Guo, B. Hurley, F. Yang, R. Buchheit, A Novel Organic Conversion Coating based on N-Benzoyl-N-Phenylhydroxylamine Chemistry for the Corrosion Protection of AA2024-T3, Electrochimica Acta, 246 (2017) 197-207.
[36] R.G. Kelly, Crevice corrosion, Encyclopedia of Electrochemistry, 4 (2007) 275.
[37] E. Desimoni, C. Malitesta, P. Zambonin, J. Riviere, An x-ray photoelectron spectroscopic study of some chromium–oxygen systems, Surface and interface analysis, 13 (1988) 173-179.
[38] I. Ikemoto, K. Ishii, S. Kinoshita, H. Kuroda, M.A. Franco, J. Thomas, X-ray photoelectron spectroscopic studies of CrO2 and some related chromium compounds, Journal of Solid State Chemistry, 17 (1976) 425-430.
[39] G. Allen, P. Tucker, Multiplet splitting of X-ray photoelectron lines of chromium complexes. The effect of covalency on the 2p core level spin-orbit separation, Inorganica Chimica Acta, 16 (1976) 41-45.
[40] S. Contarini, S. Aduru, J. Rabalais, Decomposition of chromate salts stimulated by ion and electron irradiation, The Journal of Physical Chemistry, 90 (1986) 3202-3205.

[41] J. Haber, T. Machej, L. Ungier, J. Ziółkowski, ESCA studies of copper oxides and copper molybdates, Journal of Solid State Chemistry, 25 (1978) 207-218.
[42] E. Deltombe, N. de Zoubov, M. Pourbaix, Atlas of electrochemical equilibria in aqueous solutions, (1966) 272-279.
[43] R. Poole, P. Kemeny, J. Liesegang, J. Jenkin, R. Leckey, High resolution photoelectron studies of the d bands of some metals, Journal of Physics F: Metal Physics, 3 (1973) L46.
[44] J.-G. Choi, L. Thompson, XPS study of as-prepared and reduced molybdenum oxides, Applied surface science, 93 (1996) 143-149.
[45] N. McIntyre, D. Johnston, L. Coatsworth, R. Davidson, J. Brown, X-ray photoelectron spectroscopic studies of thin film oxides of cobalt and molybdenum, Surface and interface analysis, 15 (1990) 265-272.
[46] Y. Lu, C. Clayton, An XPS study of the passive and transpassive behavior of molybdenum in deaerated 0.1 M HCl, Corrosion science, 29 (1989) 927-937.
[47] C.F. Baes, R.S. Mesmer, The Hydrolysis of Cations, John Wiley & Sons, New York, London, Sydney, Toronto, 1976.
[48] J. Oldfield, W. Sutton, Crevice corrosion of stainless steels: I. A mathematical model, British corrosion journal, 13 (1978) 13-22.
[49] P. Lei, K. Yang, T. Shi, M. Wei, G. Ran, C. Lu, Surface Alteration and Chemical Durability of Hollandite (Cr, Al and Ti) Consolidated by Spark Plasma Sintering in Acid Solution, J. Nucl. Mater., Submitted (2022).
[50] G. Salamat, G. Juhl, R. Kelly, Mechanism of dissimilar metal crevice corrosion of superferritic stainless steels, Corrosion, 51 (1995) 826-836.
[51] J. Oldfield, W. Sutton, Crevice corrosion of stainless steels: II. Experimental studies, British Corrosion Journal, 13 (1978) 104-111.
[52] R.S. Lillard, S. Mehrazi, Quantifying Alloy 625 Crevice Corrosion using an Image Differencing Technique: Part III, The Transition from Diffusion to Activation Control and the Implications for the Measured Electrochemical Potentials, J. Electrochem. Soc., 168 (2021) 021511.
[53] R.S. Lillard, S. Mehrazi, D.M. Miller, Quantifying Alloy 625 Crevice Corrosion Using an Image Differencing Technique: Part I. Initiation and Propagation, J. Electrochem. Soc., 167 (2020) 021511.
[54] S.D. Cramer, The solubility of oxygen in brines from 0 to 300 C, Industrial & Engineering Chemistry Process Design and Development, 19 (1980) 300-305.
[55] F. Torabi, P. Ahmadi, Chapter 1-Battery technologies, Simulation of Battery Systems, (2020) 1-54.

a

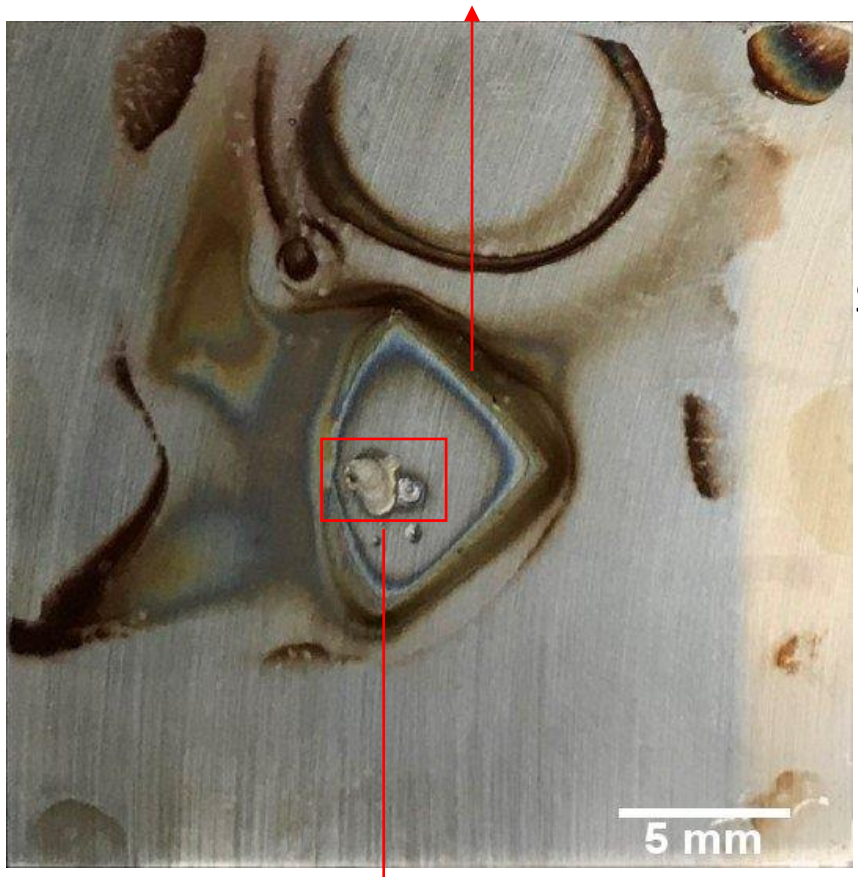
Boundary of contact area
5 mm

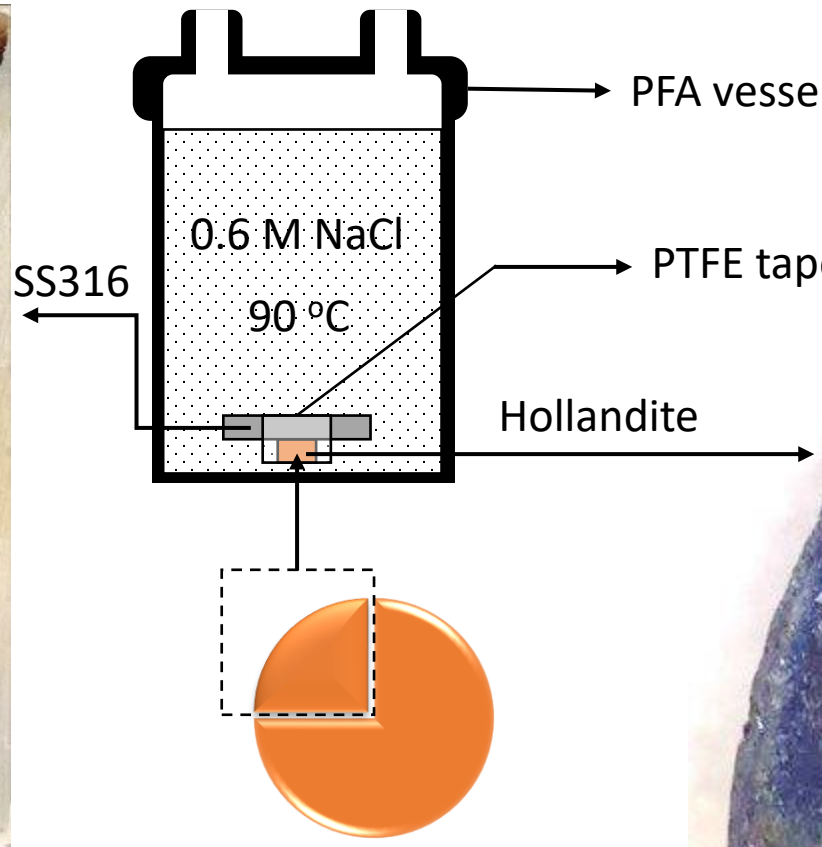
PFA vessel
0.6 M NaCl
90 °C
SS316
PTFE tape
Hollandite

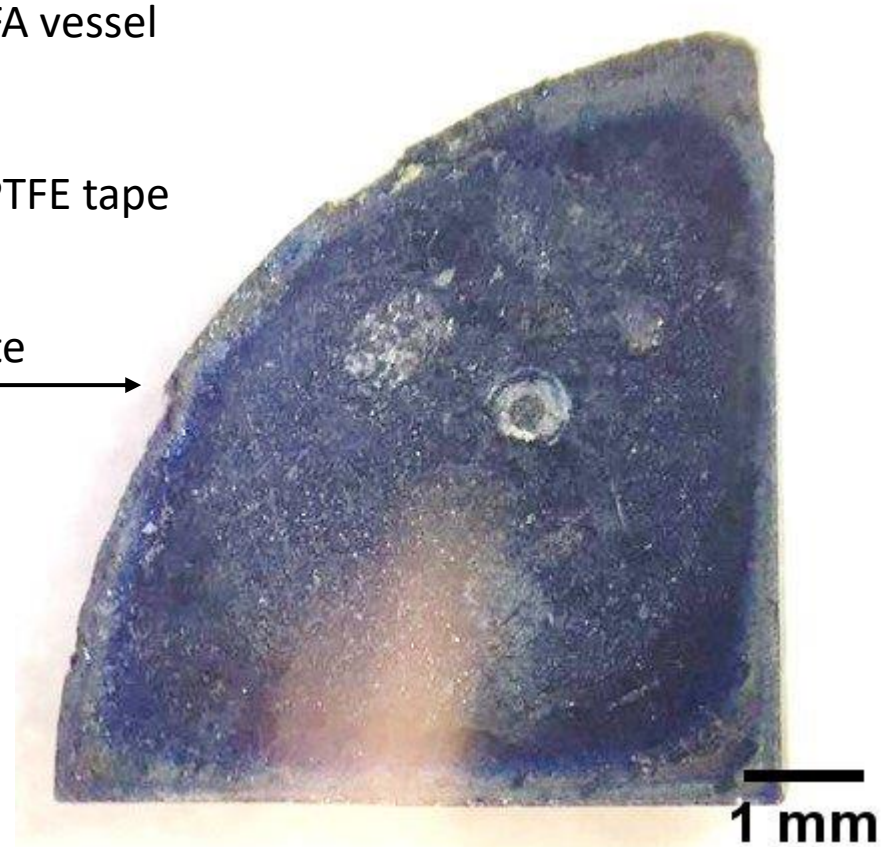
1 mm

b

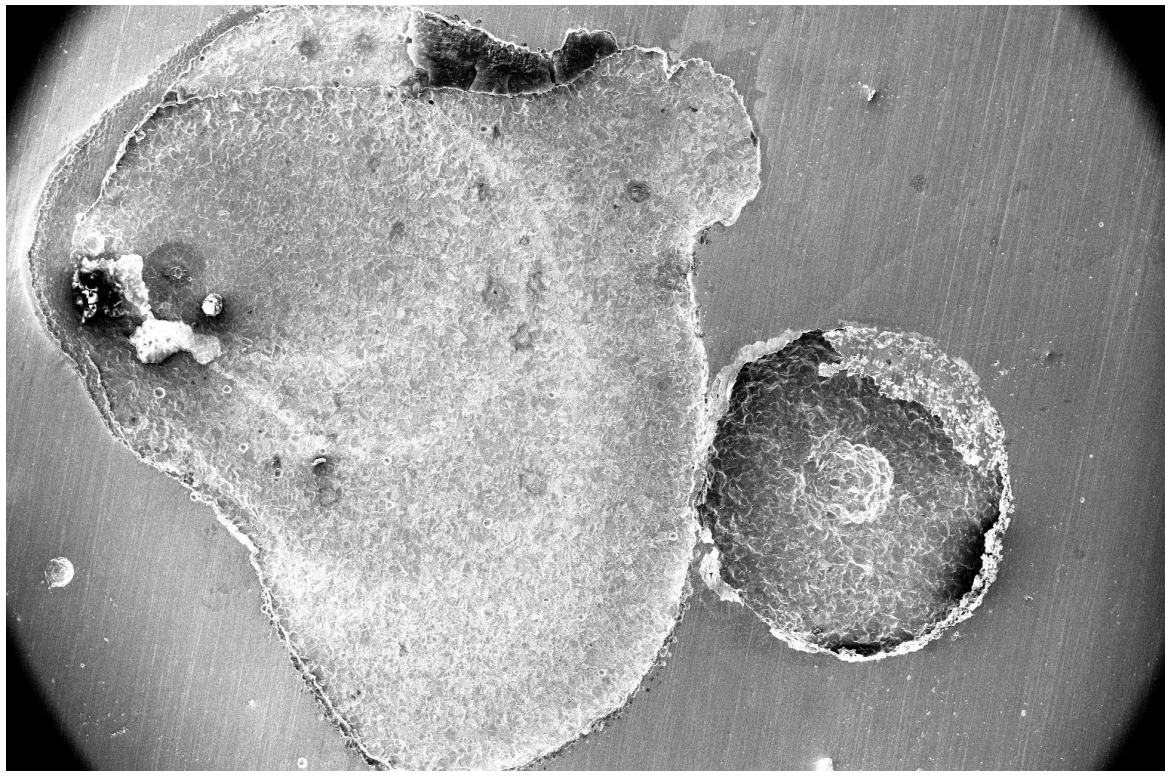
500 µm

c

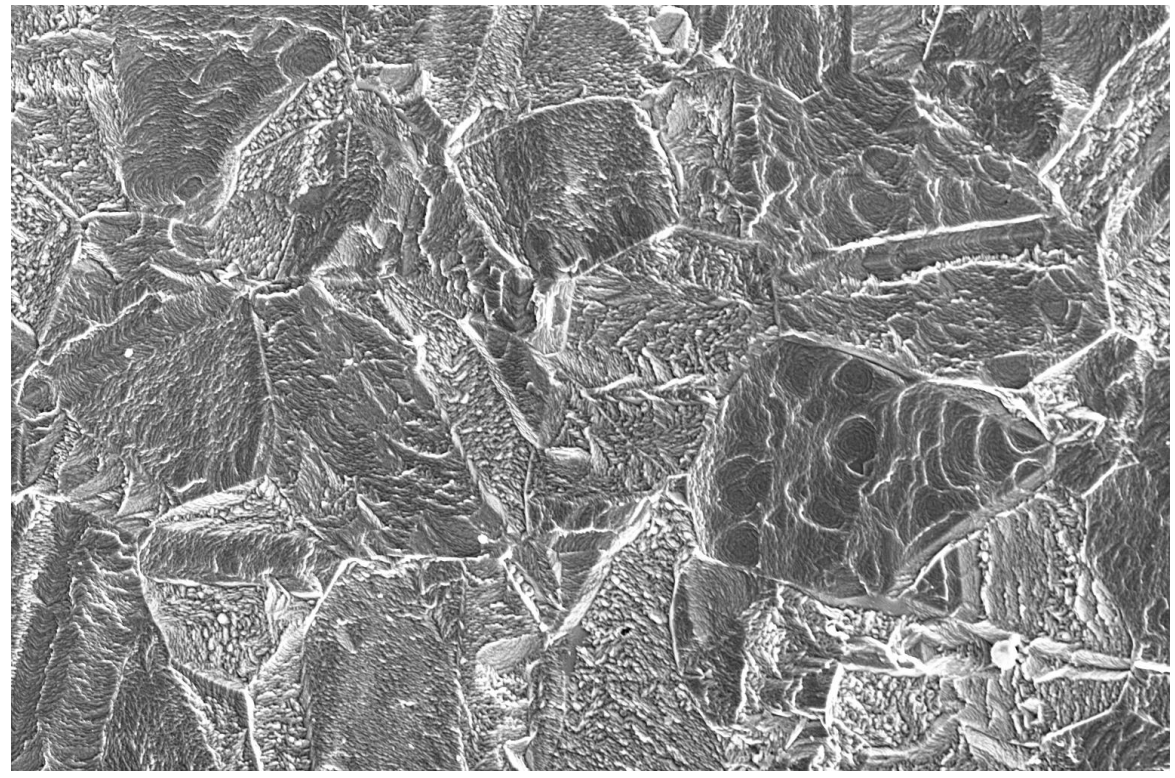
20 µm

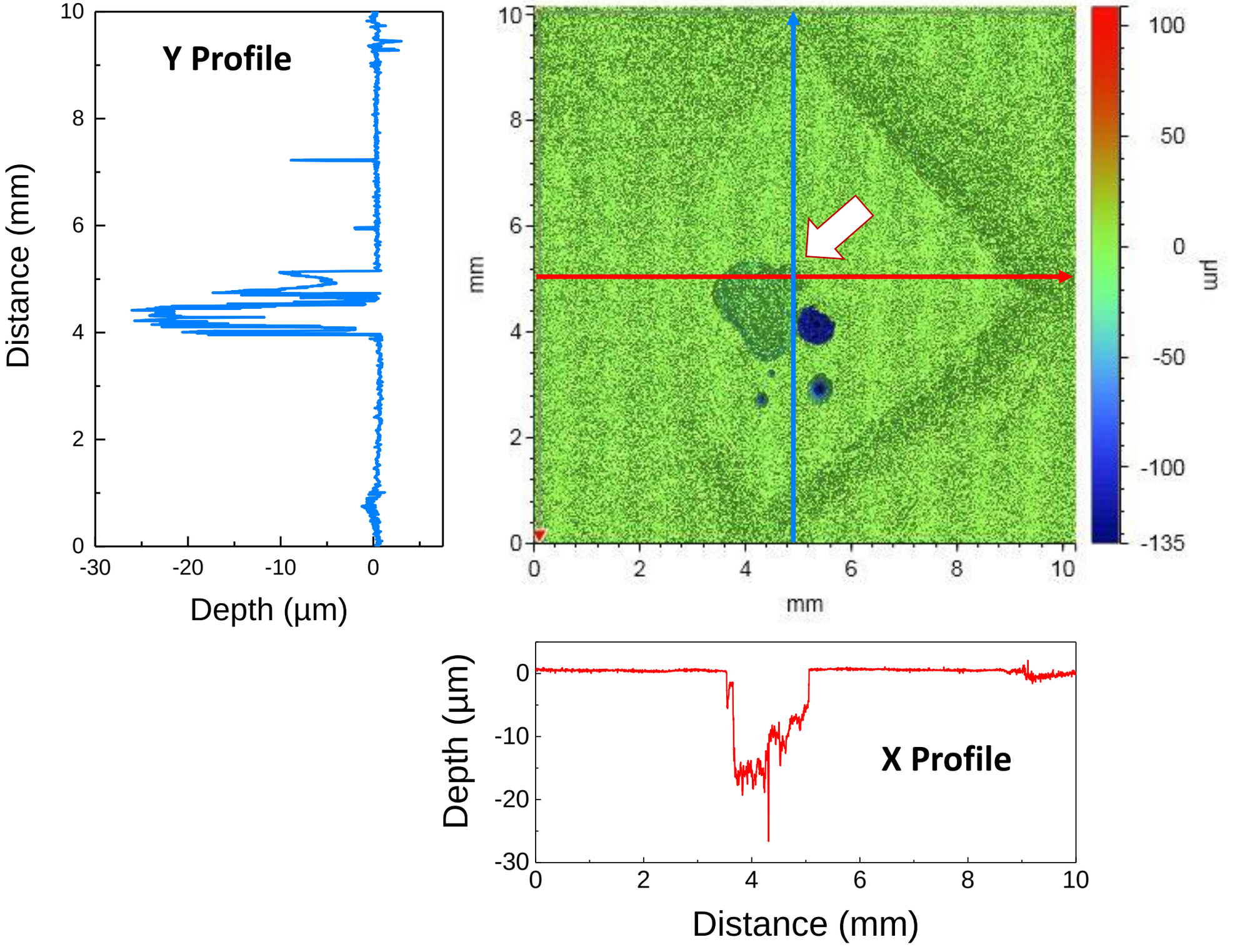
Y Profile
Distance (mm)
Depth (µm)
10
8
6
4
2
0
-30
-20
-10
0
mm
mm
µm
100
50
0
-50
-100
-135
X Profile
Depth (µm)
Distance (mm)

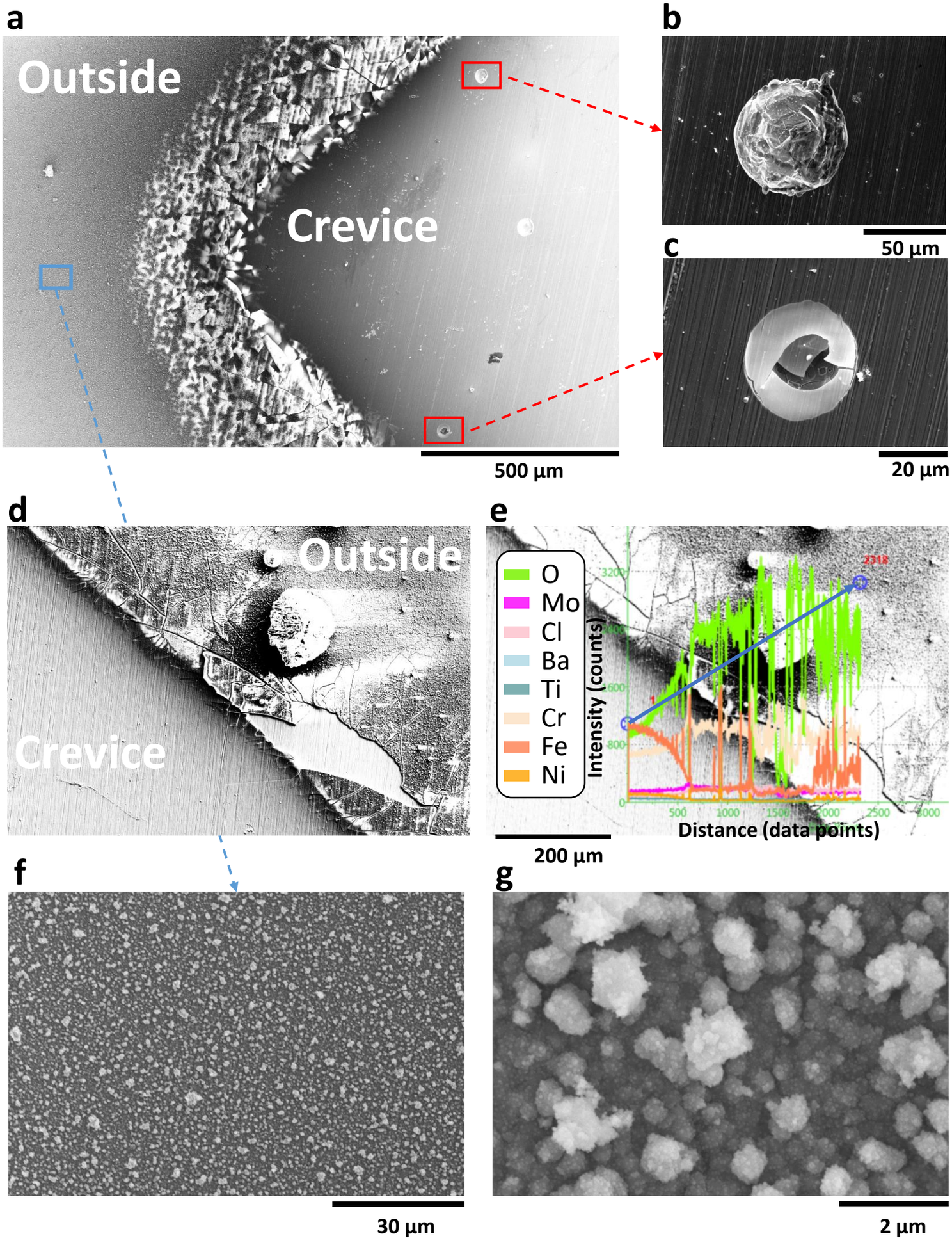
a
Outside
Crevice
500 µm
b
50 µm
c
20 µm
d
Outside
Crevice
e
O
Mo
Cl
Ba
Ti
Cr
Fe
Ni
Intensity (counts)
Distance (data points)
200 µm
f
30 µm
g
2 µm

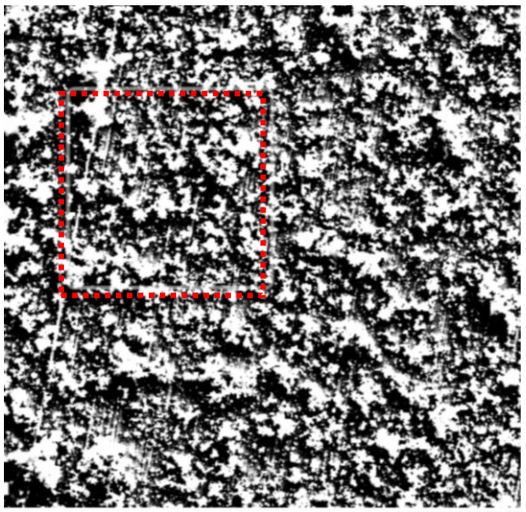

O

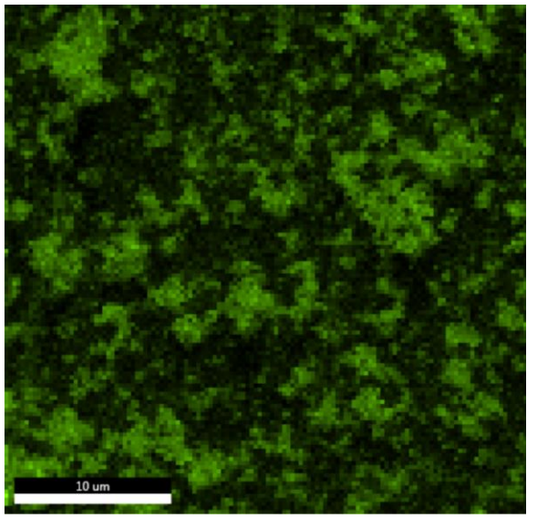

Ba

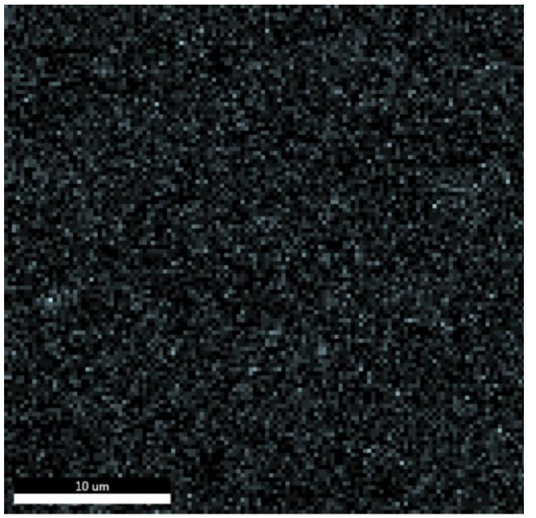

Fe

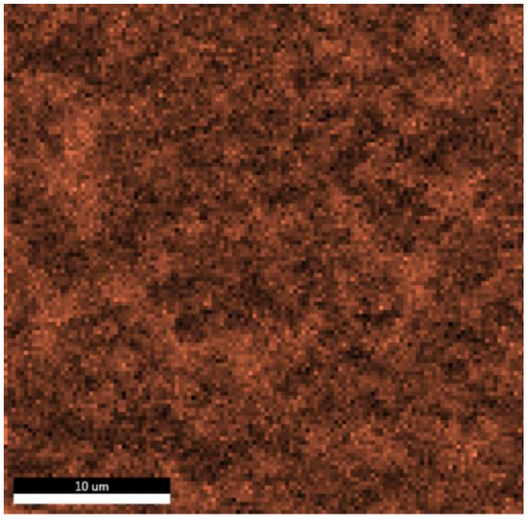

Cr

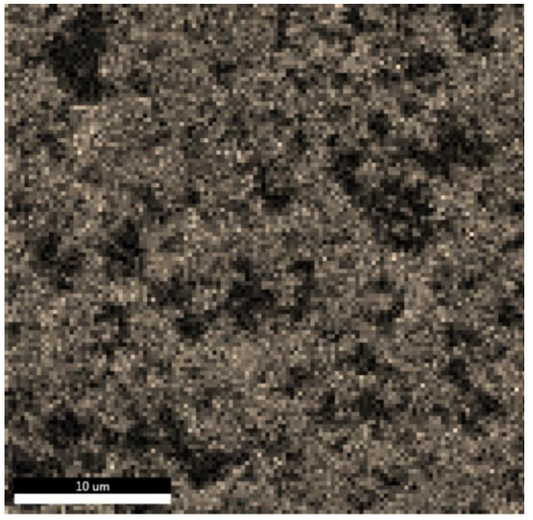

Ni

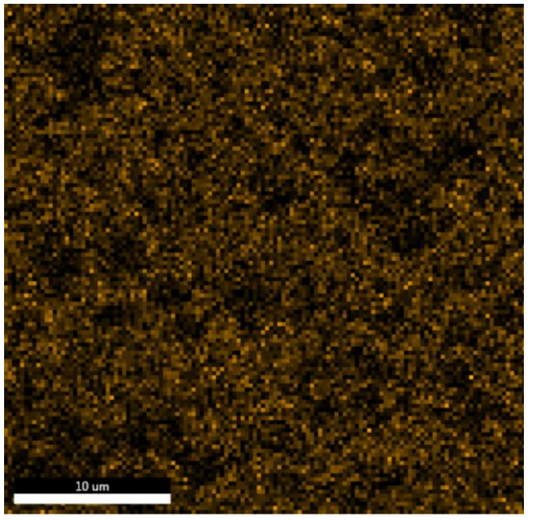

Mo

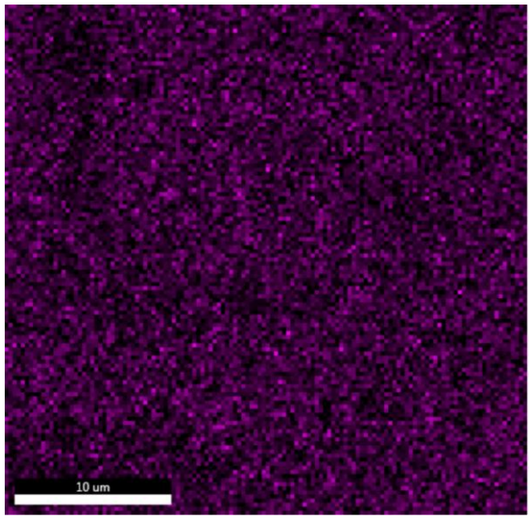

Cl

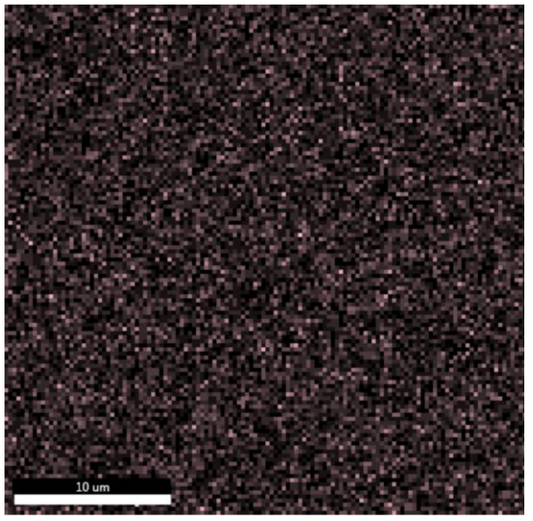

Overlap

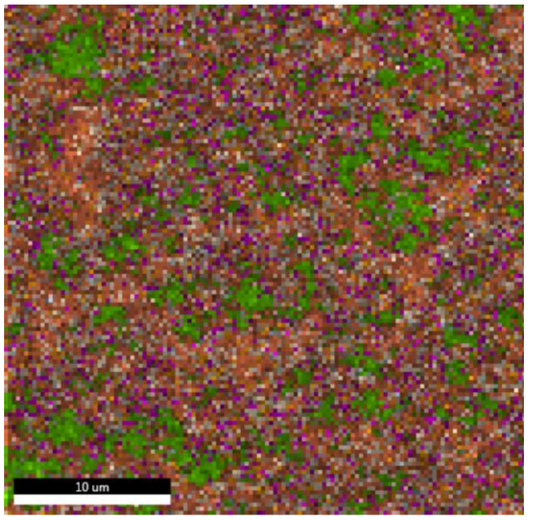

10 µm

a

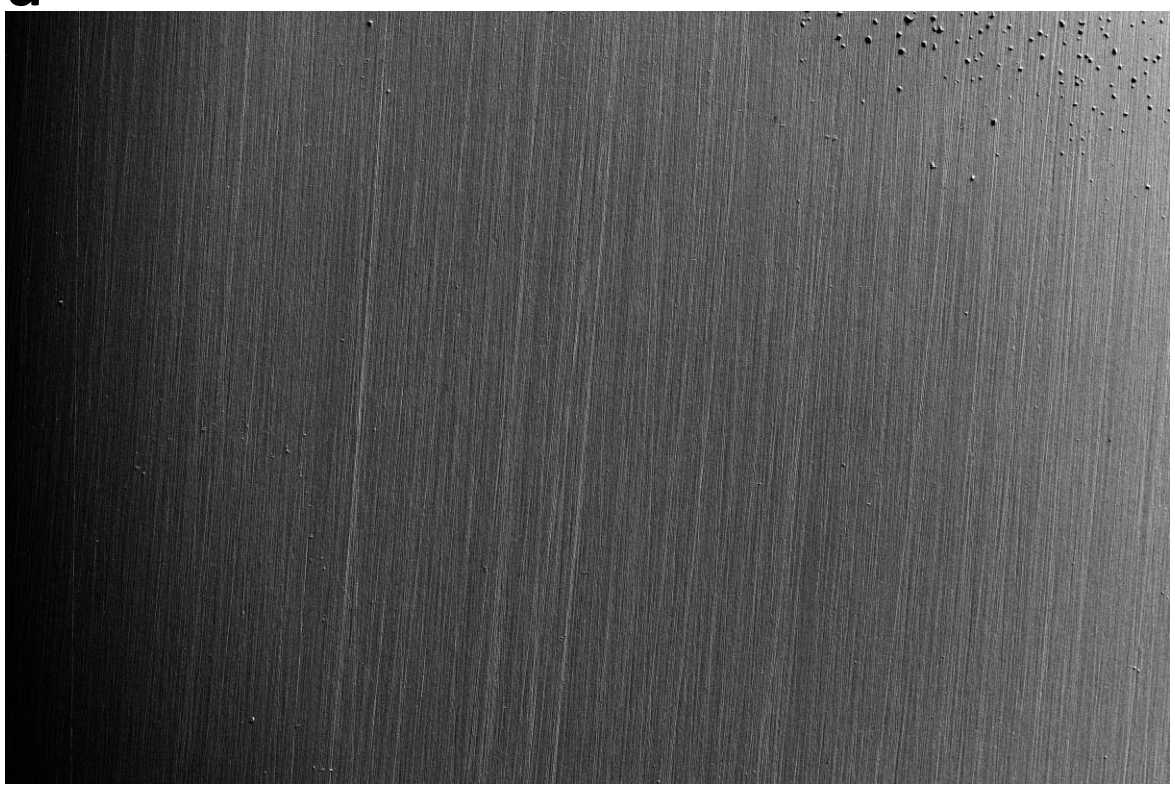

500 µm

b

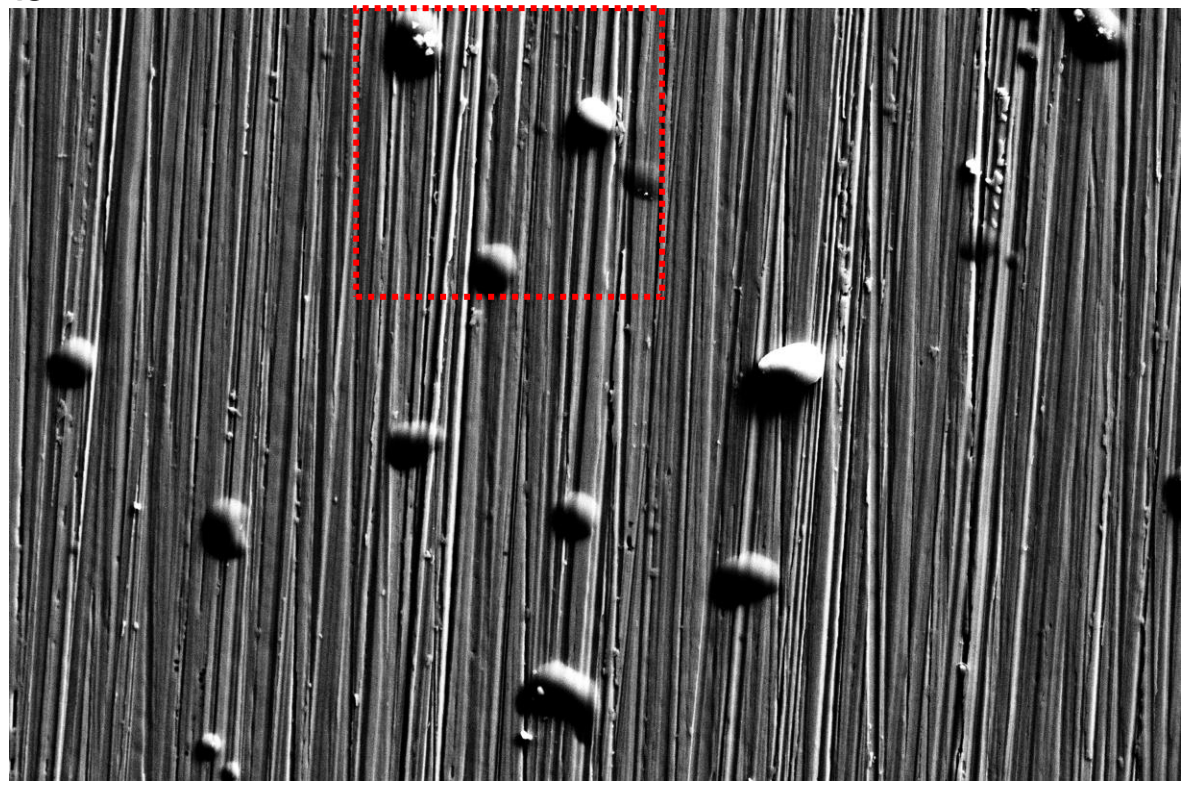

40 µm

c

C

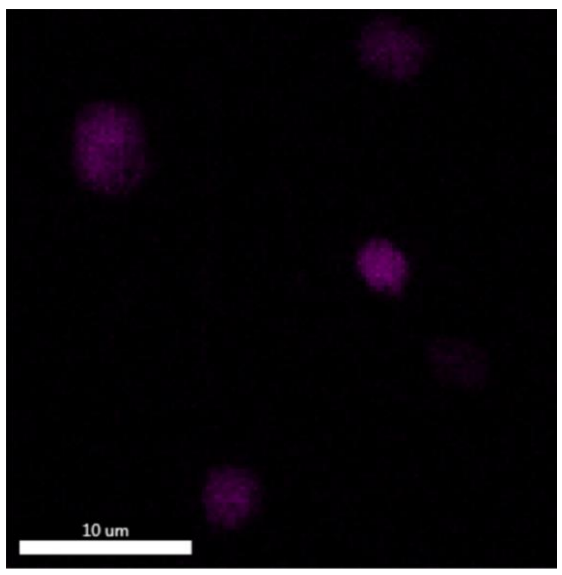

O

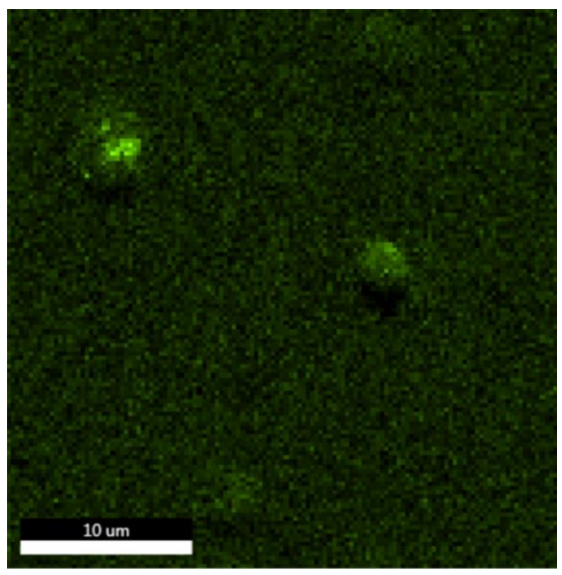

Al

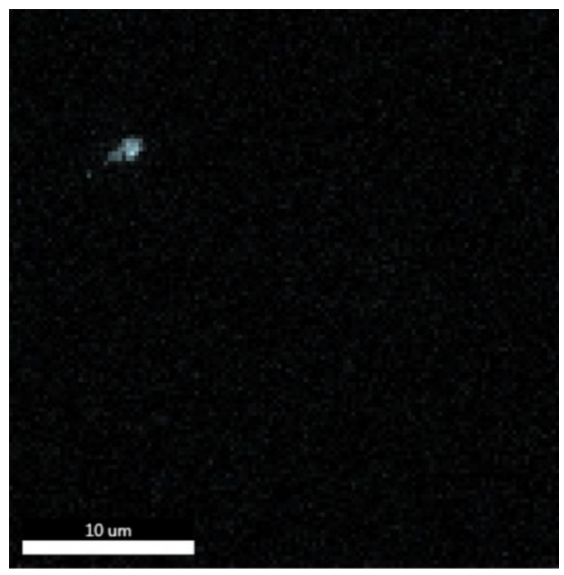

Ba

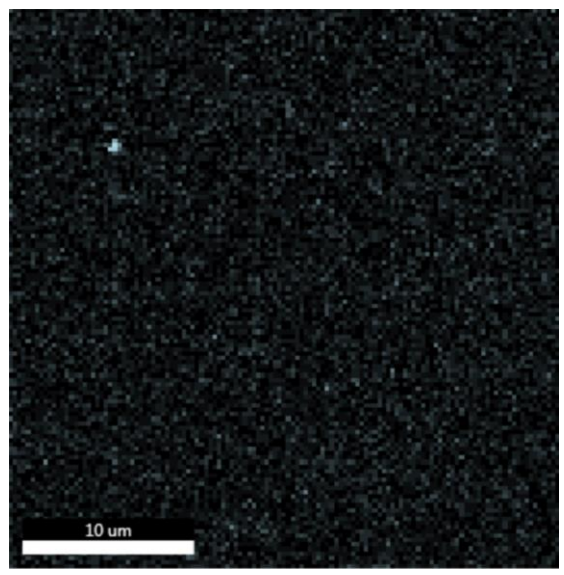

Fe

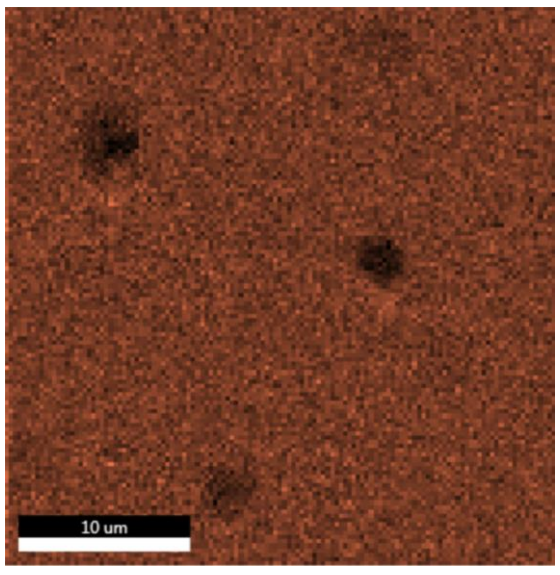

Cr

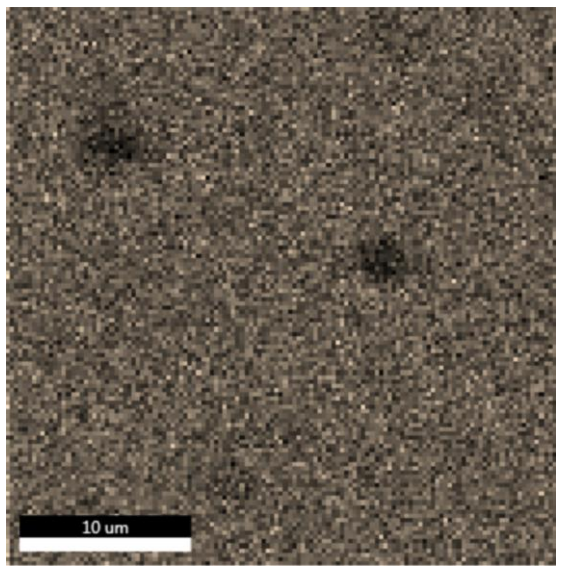

Ni

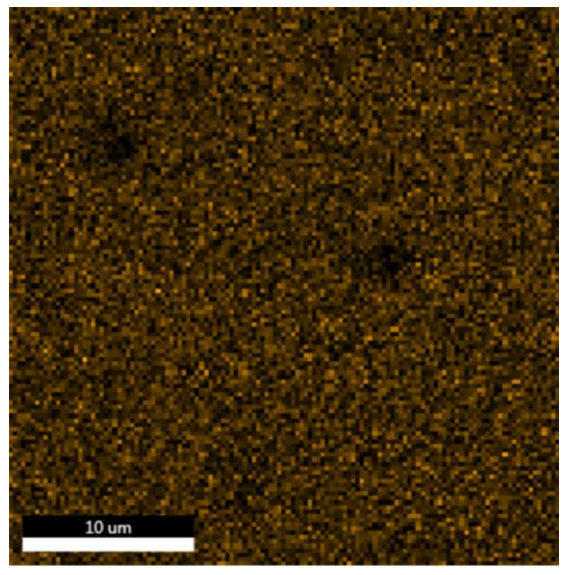

Mo

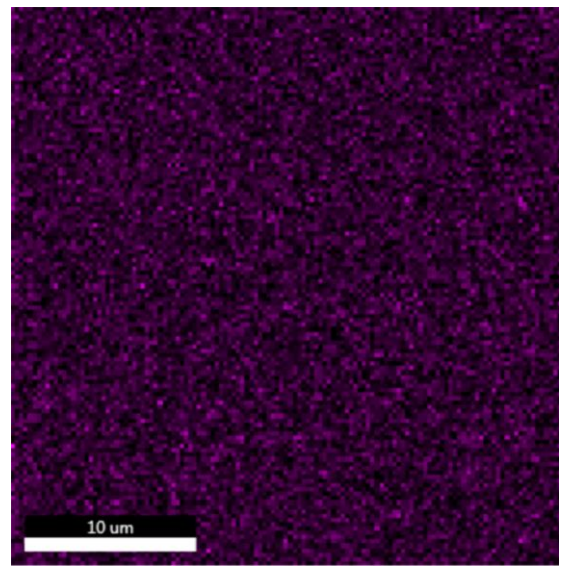

10 µm

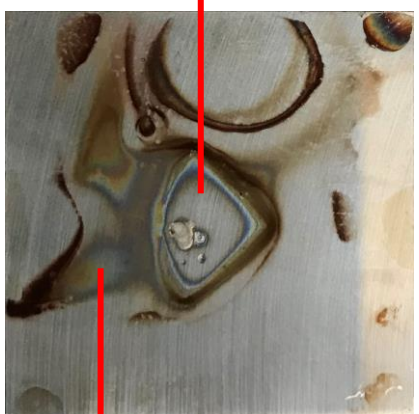
Crevice
Bulk

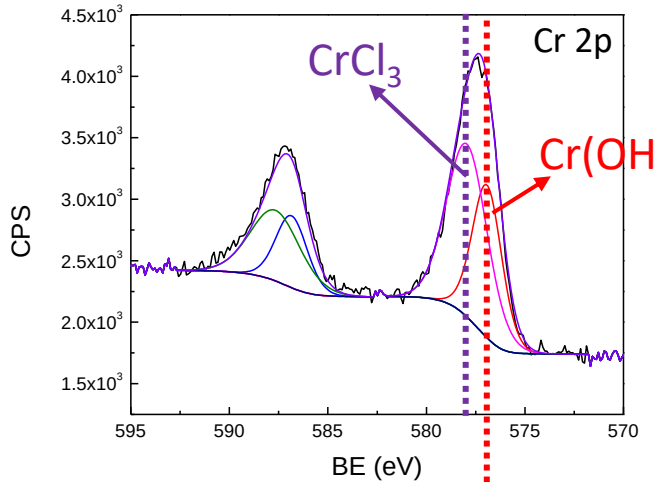
Cr 2p
$CrCl_3$
$Cr(OH)_3$
CPS
BE (eV)

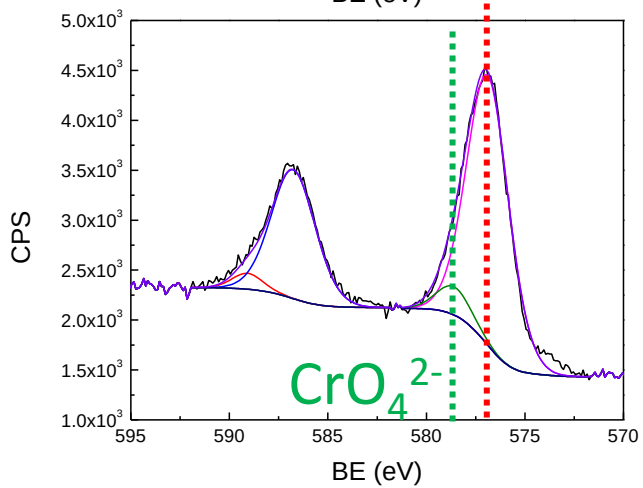
CrO_4^{2-}
CPS
BE (eV)

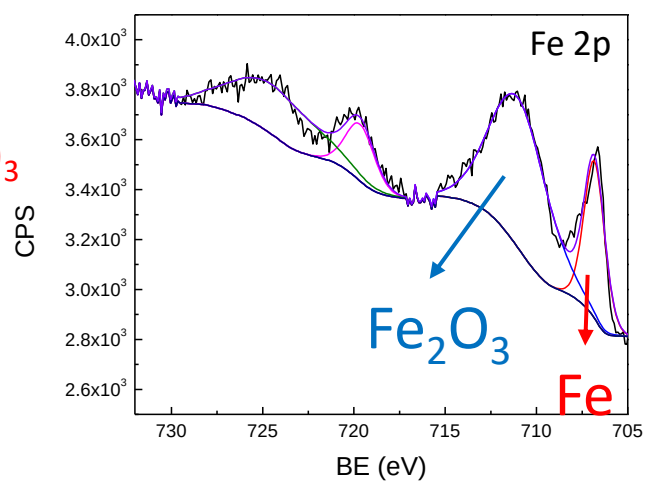
Fe 2p
Fe_2O_3
Fe
CPS
BE (eV)

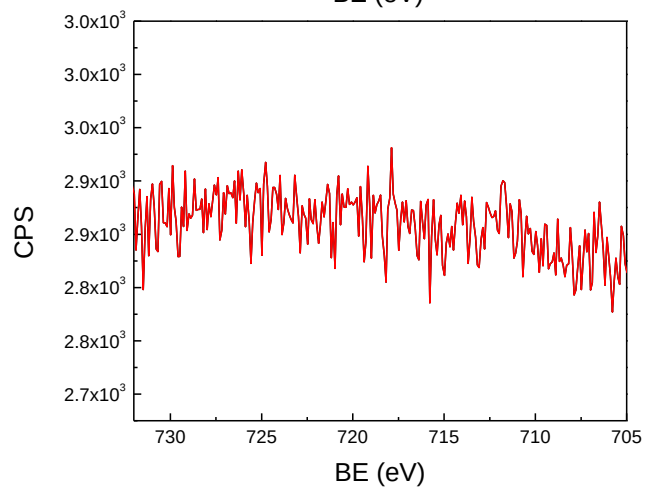
CPS
BE (eV)

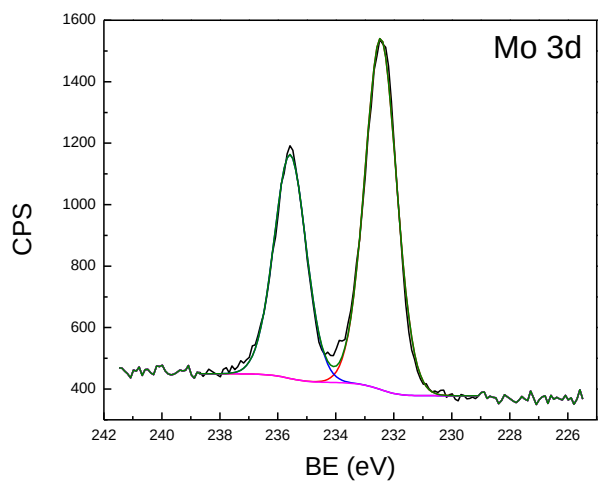
Mo 3d
CPS
BE (eV)

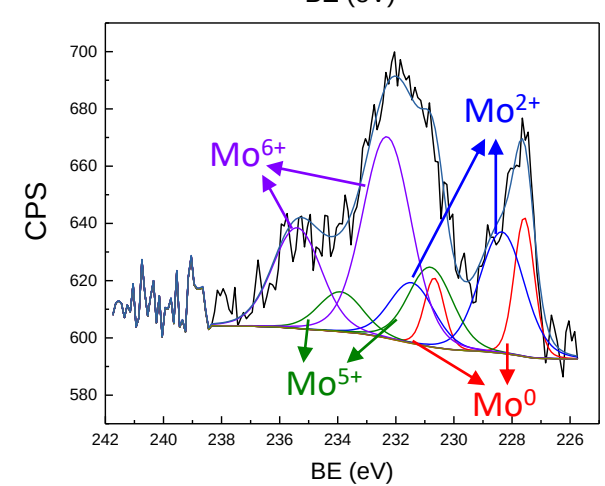
Mo^{6+}
Mo^{2+}
Mo^{5+}
Mo^{0}
CPS
BE (eV)

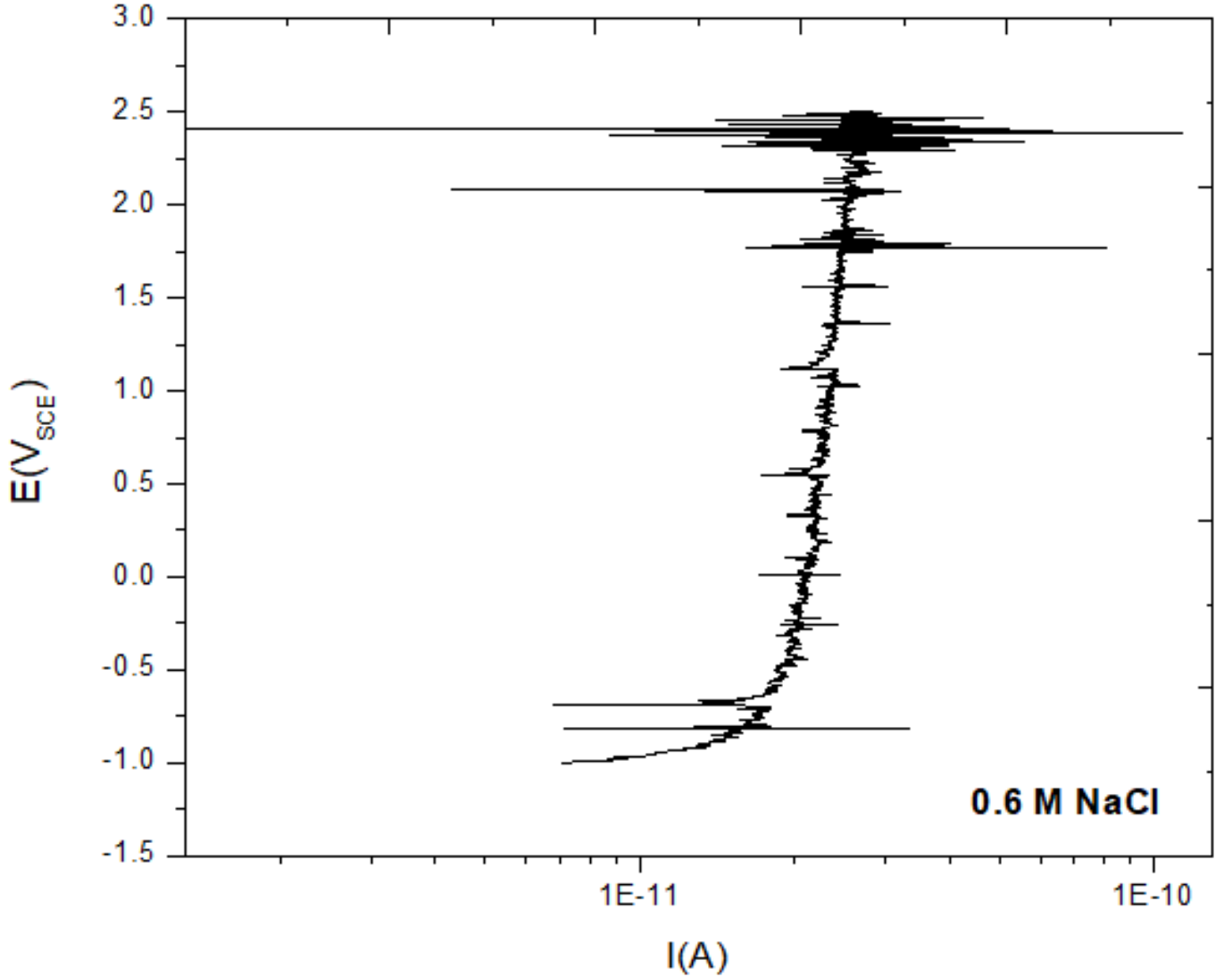
3.0
2.5
2.0
1.5
1.0
0.5
0.0
-0.5
-1.0
-1.5
E(V_SCE)
1E-11
1E-10
I(A)
0.6 M NaCl

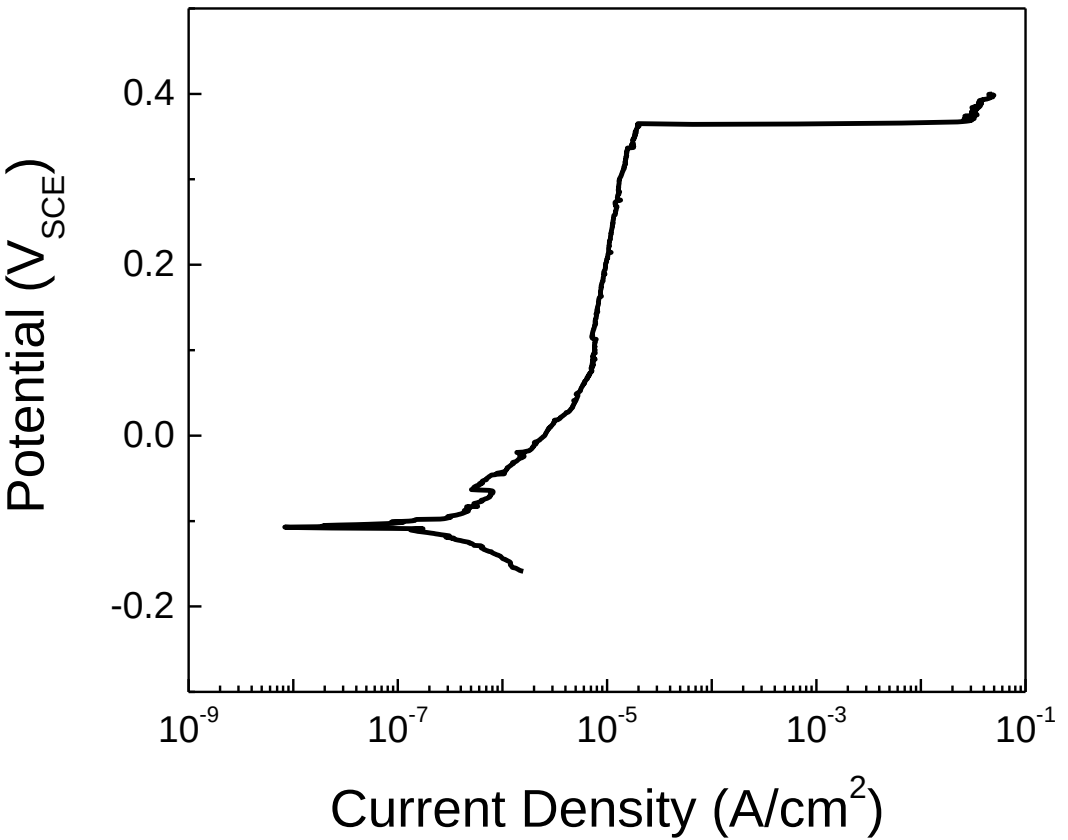
0.4
0.2
0.0
-0.2
Potential (V_{SCE})
10^{-9}
10^{-7}
10^{-5}
10^{-3}
10^{-1}
Current Density (A/cm^2)

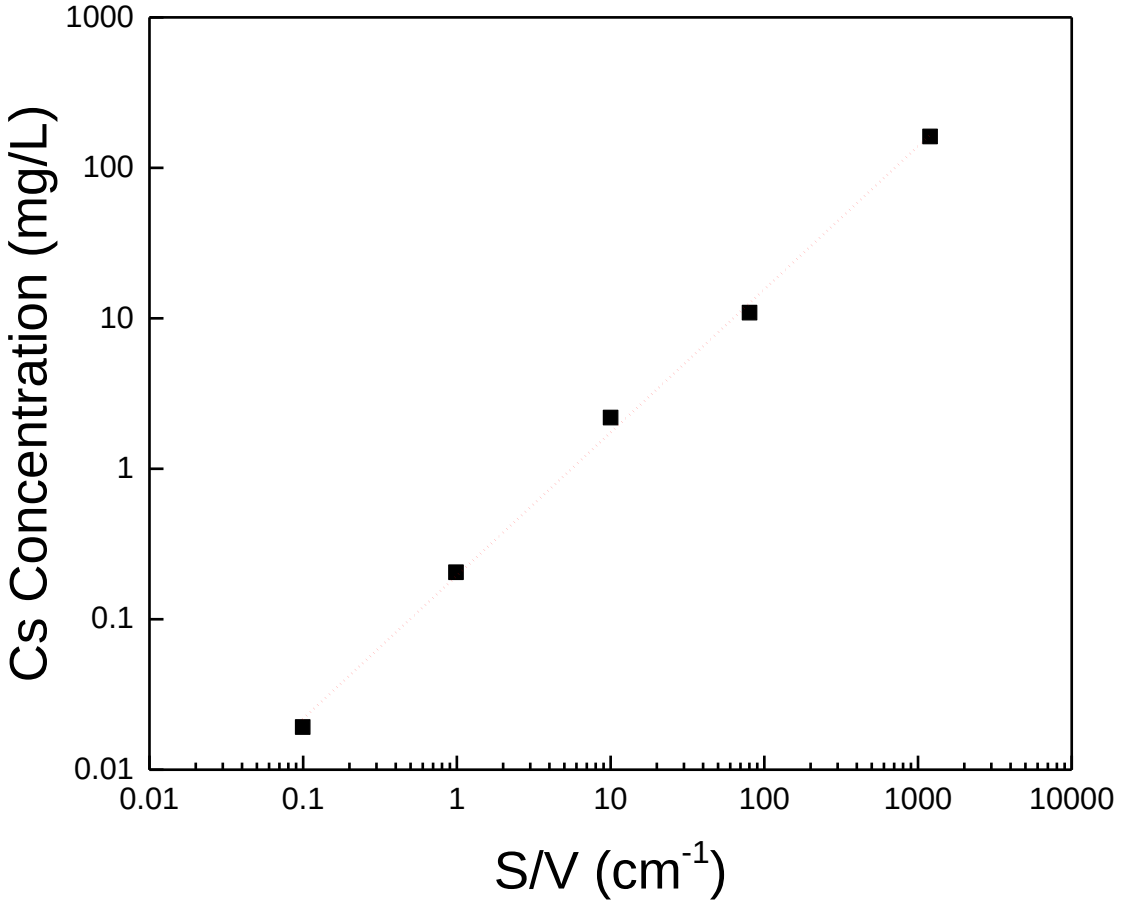
Cs Concentration (mg/L)
1000
100
10
1
0.1
0.01
0.01
0.1
1
10
100
1000
10000
S/V (cm-1)

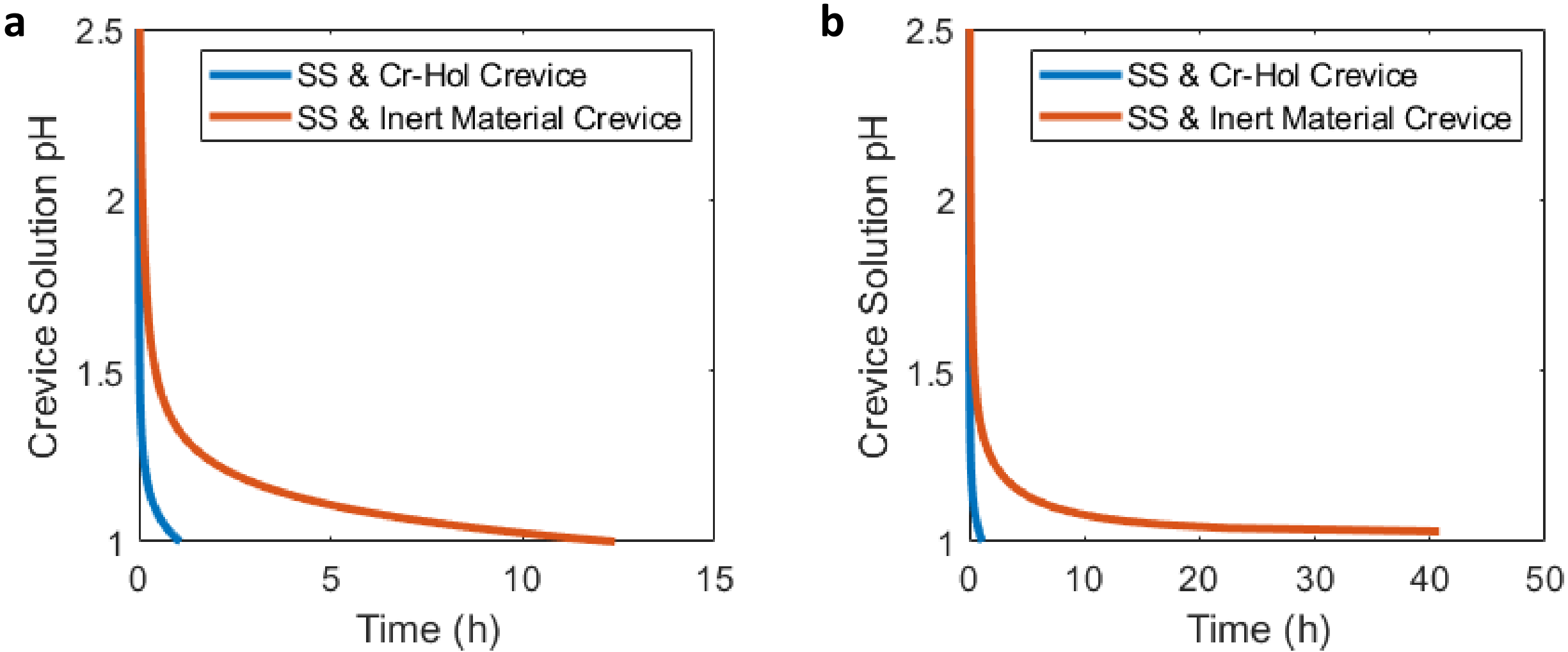
a
b
SS & Cr-Hol Crevice
SS & Inert Material Crevice
Crevice Solution pH
Time (h)
2.5
2
1.5
1
0
5
10
15
20
30
40
50

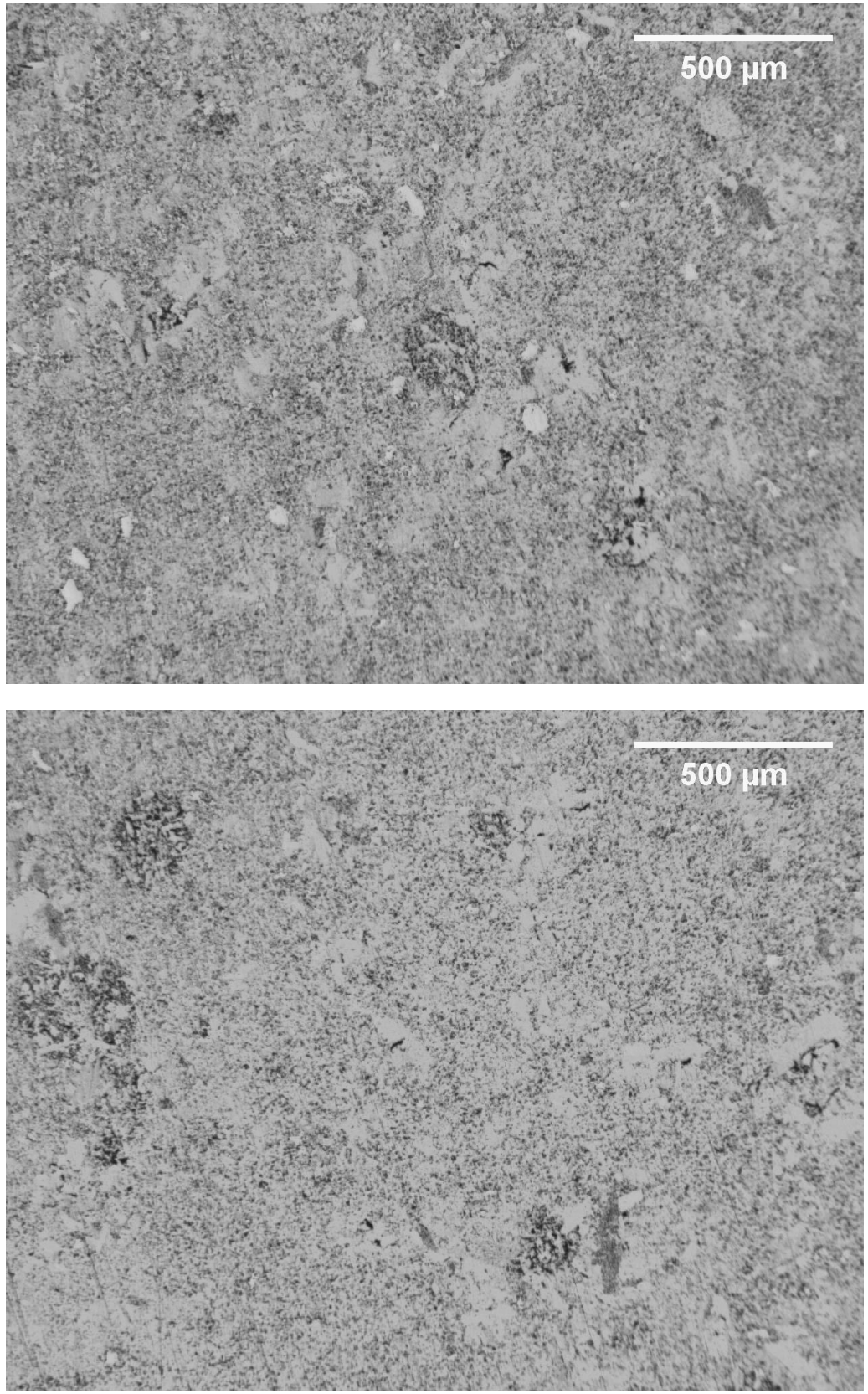
500 µm

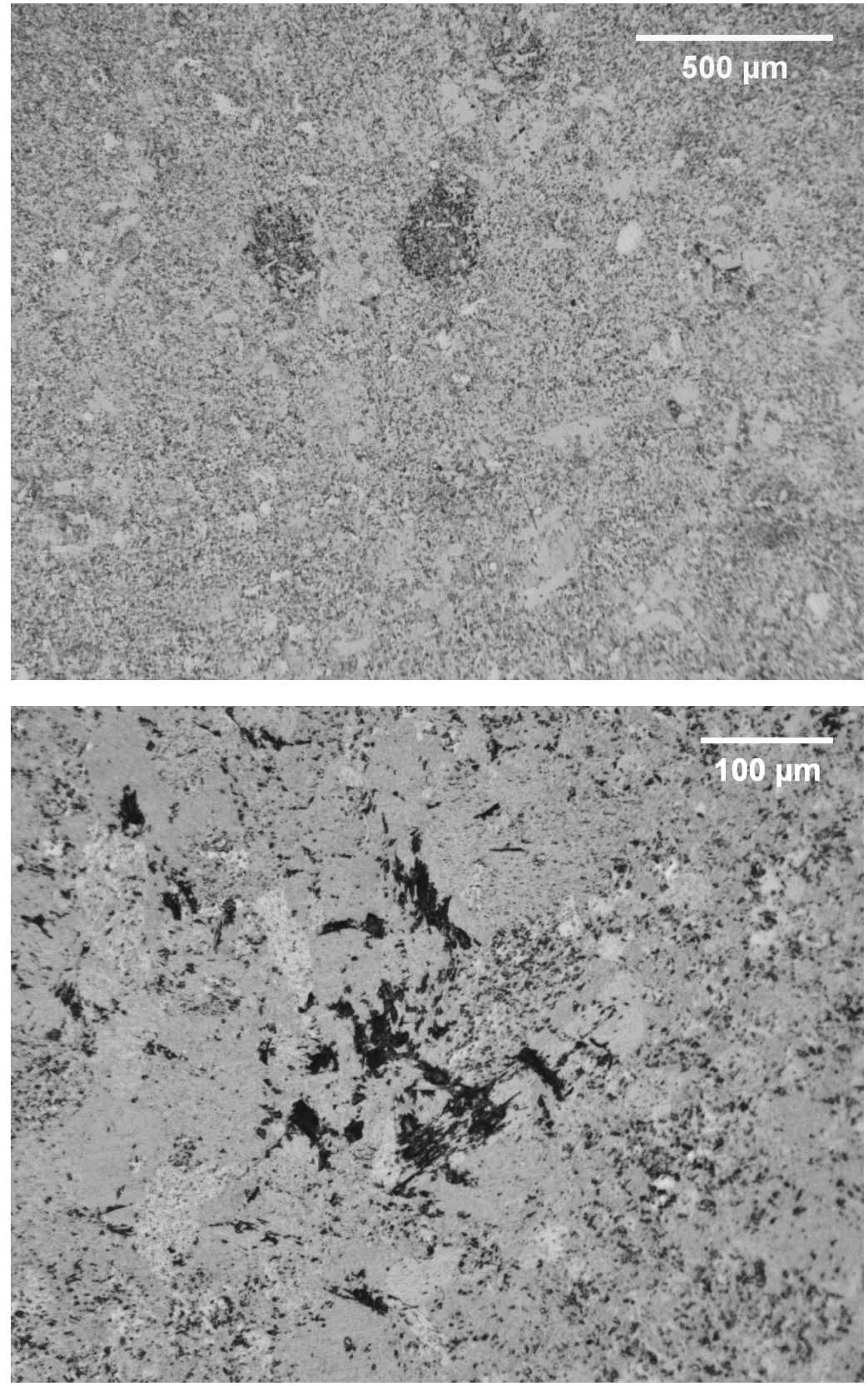
500 µm

500 µm

100 µm

a

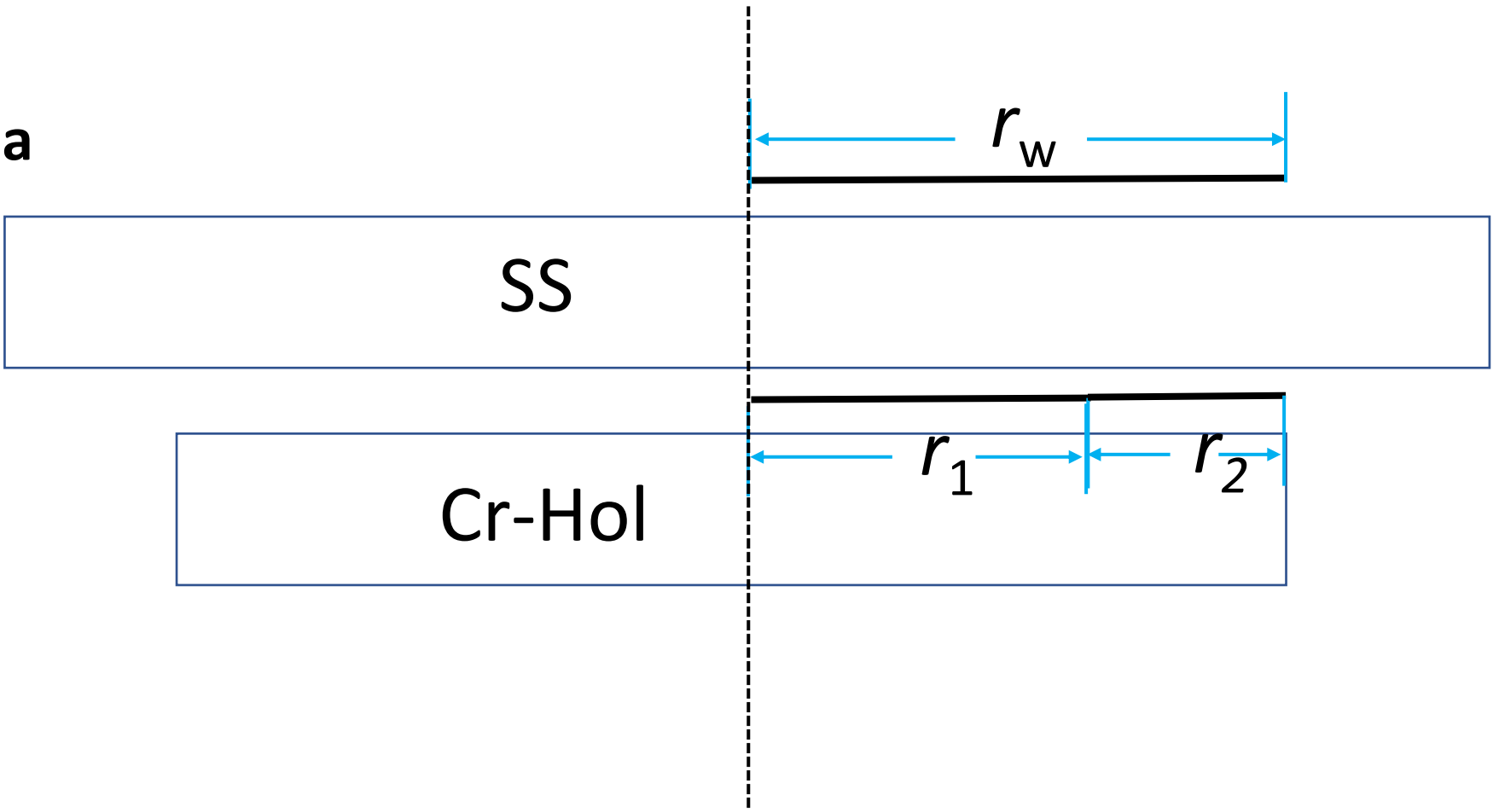

b